

1 **Properties of Ion-Inertial Scale Plasmoids Observed by the Juno Spacecraft in the**
2 **Jovian Magnetotail**

3

4 **Enter authors here:**

5 **Yash Sarkango¹, James A. Slavin¹, Xianzhe Jia¹, Gina A. DiBraccio², George B. Clark³,**
6 **Weijie Sun¹, Barry H. Mauk³, William S. Kurth⁴, and George B. Hospodarsky⁴**

7 ¹University of Michigan - Ann Arbor, USA.

8 ²NASA Goddard Space Flight Center, USA.

9 ³John Hopkins University – Applied Physics Laboratory, USA

10 ⁴University of Iowa, USA

11

12 Corresponding author: Yash Sarkango (sarkango@umich.edu)

13

14 **Key Points:**

- 15 • We identify and analyze 87 ion-inertial scale plasmoids (56 O-lines, 31 flux-ropes) in the
16 Jovian magnetotail using an automated algorithm.
- 17 • North-South field reversals with peak-to-peak durations less than 60 s are more common
18 than those with durations between 60 and 300 s.
- 19 • Ion-inertial scale plasmoids alone cannot account for the >500 kg/s loss-rate deficit
20 unless they are being produced every ~0.1 s or less.

21 **Abstract**

22 We expand on previous observations of magnetic reconnection in Jupiter's magnetosphere by
 23 constructing a survey of ion-inertial scale plasmoids in the Jovian magnetotail. We developed an
 24 automated detection algorithm to identify reversals in the B_θ component and performed the
 25 minimum variance analysis for each identified plasmoid to characterize its helical structure. The
 26 magnetic field observations were complemented by data collected by the Juno Waves instrument,
 27 which is used to estimate the total electron density, and the JEDI energetic particle detectors. We
 28 identified 87 plasmoids with 'peak-to-peak' durations between 10 s and 300 s. 31 plasmoids
 29 possessed a core field and were classified as flux-ropes. The other 56 plasmoids had minimum
 30 field strength at their centers and were termed O-lines. Out of the 87 plasmoids, 58 had in situ
 31 signatures shorter than 60 s, despite the algorithm's upper limit to be 300 s, suggesting that smaller
 32 plasmoids with shorter durations were more likely to be detected by Juno. We estimate the
 33 diameter of these plasmoids assuming a circular cross-section and a travel speed equal to the
 34 Alfvén speed in the surrounding lobes. Using the electron density inferred by Waves, we contend
 35 that these plasmoid diameters were within an order of the local ion-inertial length. Our results
 36 demonstrate that magnetic reconnection in the Jovian magnetotail occurs at ion scales like in other
 37 space environments. We show that ion-scale plasmoids would need to be released every 0.1 s or
 38 less to match the canonical 1 ton/s rate of plasma production due to Io.

39 **1. Introduction**

40 Magnetic reconnection can be the primary mechanism through which the plasma created
 41 in Jupiter's inner magnetosphere from Io and Europa is ultimately lost to the external solar wind
 42 (Vasyliunas, 1983; Krupp et al., 2004). Many in situ observations support this hypothesis through
 43 different particle and field signatures, which are briefly summarized in the following paragraphs.

44 Recurring bursts of energetic particles occur in the Jovian magnetotail with flow velocities
 45 deviating from the corotation direction (Krimigis et al., 1981; Krupp et al., 1998; Woch et al.,
 46 2002; Kronberg et al., 2005, 2007; Kronberg, Woch, Krupp, & Lagg, 2008; Kasahara et al., 2013).
 47 These flow bursts repeat on timescales between 1 to 4 days and can be directed either inward
 48 (sunward) or outward (anti-sunward). More inward flow bursts are seen at radial locations closer
 49 to Jupiter, whereas outward bursts are common farther away from the planet (Woch et al., 2002).
 50 They are associated with an increase in the energetic particle fluxes and a decrease in the ion
 51 energy spectral index γ , or hardening of the ion energy spectra (Krupp et al., 1998; Woch et al.,
 52 1998). The peak energy of the ions also increases, which suggests acceleration associated with
 53 these events (Woch et al., 1999).

54 Simultaneous magnetic field observations have shown that flow bursts occur during
 55 periods of reversals in the north-south component of the magnetic field (Nishida, 1983; Russell et
 56 al., 1998; Woch et al., 1999; Kronberg et al., 2005; Vogt et al., 2010, 2014, 2020). Under typical
 57 quiet conditions, the magnetic field in the Jovian magnetotail points predominantly southward at
 58 the magnetic equator. Abrupt north-south reversals indicate a change in the topology through
 59 magnetic reconnection. Persistent northward magnetic fields may indicate open magnetic flux that
 60 is 'disconnected' from Jupiter (Vogt et al., 2014). Multiple north-south reversals can be seen within
 61 a single reconfiguration event lasting over a period of several days (Kronberg et al., 2007). The
 62 sense of the reversal, i.e., from north to south or vice-versa, provides more information about the
 63 placement of the measuring spacecraft with respect to the reconnection X-line, which can be
 64 identified based on the meridional component for a given interval (Ge et al., 2010; Vogt et al.,

65 2010). Some magnetic field reversals appear to have a helical or loop-like magnetic field structure
 66 that is characteristic of plasmoid events (Vogt et al., 2014). Also seen are magnetic signatures of
 67 ‘dipolarizations’, which are the result of plasma compression due to fast planetward flows in the
 68 so-called ‘exhausts’ emanating from the reconnection sites (Artemyev et al., 2013, 2020; Yao et
 69 al., 2020).

70 The simultaneous occurrences of magnetic field reversals and flow bursts repeating on
 71 similar timescales suggests a common origin. That such events recur over long timescales of 1-4
 72 days, with no clear dependence on solar wind triggers, also suggests an internally driven
 73 phenomenon. The dominant field component in the lobes parallel to the current sheet (B_r)
 74 gradually increases between two consecutive active periods and decreases after the onset of the
 75 events, while the opposite is true for the component normal to the current sheet (B_θ) at the equator.
 76 This implies a gradual ‘stretching’ of the magnetodisc over the 1 to 4-day period (Ge et al., 2007;
 77 Kronberg et al., 2007). Based on the above points, it is believed that the magnetosphere
 78 experiences two states – a state of ‘loading’, characterized by an increase in magnetic stresses in
 79 the magnetotail, and a state of ‘unloading’, when magnetic stresses and plasma are released from
 80 the magnetosphere via magnetic reconnection and plasmoid release.

81 Based on these observations, which are also seen in Saturn’s magnetosphere (Jackman et
 82 al., 2011; Garton et al., 2021), it is now generally believed that reconnection occurs in the Jovian
 83 magnetotail and produces plasmoids. But the question remains if plasmoids can account for the 1
 84 ton/s mass addition rate produced in the inner magnetosphere (Bagenal & Delamere, 2011).
 85 Previous estimates vary on the size of and mass carried by Jovian plasmoids. Kronberg et al.,
 86 (2008) assume plasmoid down-tail length pf $9 R_J$, thickness of $2 R_J$ and azimuthal length of 200
 87 R_J ($1 R_J = 71492$ km is the equatorial radius of Jupiter at 1 bar), and an oxygen ion density of
 88 0.025 cm^{-3} and find that ~ 50 plasmoids should be released over the unloading period (~ 1 day) to
 89 balance a 250 kg/s production, with each plasmoid contributing ~ 800 tons. Bagenal, (2007)
 90 assumes a plasmoid diameter of $25 R_J$, width of $2 R_J$ and density of 0.01 cm^{-3} and estimate the
 91 mass of each plasmoid to be ~ 500 tons, which effectively translates to a loss rate of $\sim 150 \text{ kg/s}$ if
 92 such plasmoids are released on an hourly basis. Vogt et al., (2014) consider larger plasmoid
 93 dimensions with the higher estimate of the down-tail length to be $20 R_J$, a width of $6 R_J$, a cross-
 94 tail length of $70 R_J$, and density of 0.01 cm^{-3} and calculate an upper estimate of the net loss rate to
 95 be $\sim 120 \text{ kg/s}$ based on five such plasmoids released over one day. Similarly, Cowley et al., (2015)
 96 find that the rate of 1 ton/s can only be achieved after including the large post-plasmoid plasma
 97 sheet (PPPS), which may exist for the ~ 15 h recurrence time between consecutive reconnection
 98 events and would increase effective plasmoid down-tail lengths up to $\sim 150 R_J$. Hence, isolated,
 99 and infrequent plasmoids, which recur on a timescale of several hours or days, cannot match the
 100 contribution due to the Galilean satellites without the inclusion of the PPPS. It can also be noted
 101 from the widely varying numbers shown above that the dimensions for Jovian plasmoids are not
 102 well constrained because of the inherent limitations of single point measurements. Meanwhile,
 103 other theories have also been proposed to explain the observed deficit which allow for mass loss
 104 through other means e.g., through boundary interactions at the magnetopause (Delamere &
 105 Bagenal, 2013; Masters, 2017) or through diffusive processes occurring at smaller scales than what
 106 has been detected in the past (Kivelson & Southwood, 2005).

107 Observations of magnetotail reconnection noted above have analogs in the terrestrial
 108 magnetosphere with the primary difference being that the driving mechanism to stress the
 109 magnetotail in the terrestrial case is the external solar wind and interplanetary magnetic field

(Kronberg, Woch, Krupp, Lagg, et al., 2008). Our understanding of magnetic reconnection and plasmoids has improved with multi-spacecraft observations in the terrestrial magnetosphere, high cadence instrumentation and kinetic simulations. Plasmoids in the terrestrial magnetosphere and other regions of the space environment are often accompanied with a strong core field within the helical magnetic structure and are called magnetic flux-ropes (Slavin et al., 2003). The magnetic pressure of the core region balances the magnetic tension force exerted by the outer regions and in some cases, plasma pressure gradients are unnecessary to maintain this quasi-equilibrium. Flux-ropes in which pressure gradients are negligible and where the magnetic forces are self-balancing are referred to as ‘force-free’. It has been argued that the force-free configuration contains minimum magnetic energy for helical structures (Taylor, 1974; Priest, 2011) toward which they tend to evolve with time. Hence, knowledge about a particular flux-rope event’s magnetic structure could be used to determine its stage of evolution. Simultaneous energetic particle observations have shown that flux-ropes which are produced on the ion-inertial scale can interact with or trap electrons and ions, which get accelerated due to adiabatic processes such as due to the conservation of the adiabatic invariants, or through non-adiabatic processes such as electromagnetic turbulence (Grigorenko et al., 2015; Kronberg et al., 2019). Evidence exists for both Fermi and betatron acceleration, which manifest as increases in the electron fluxes in the parallel and perpendicular directions, respectively (Zhong et al., 2020; Vaivads et al., 2021). Similar results are found in particle-in-cell simulations (Drake et al., 2006).

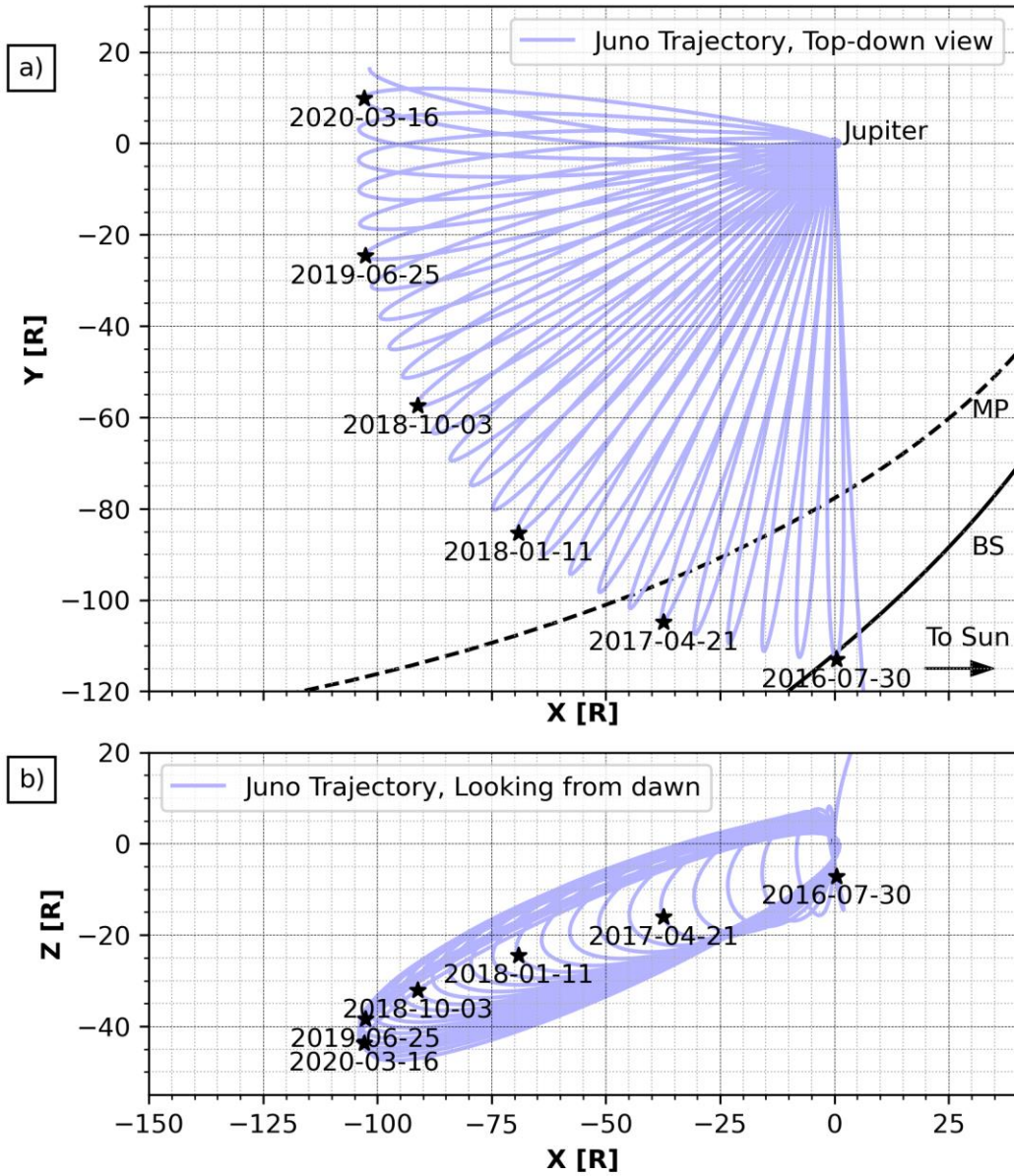
Plasmoids observed in the Jovian magnetotail have predominantly contained minimum magnetic field strength in their interiors and are not force-free flux-ropes (Vogt et al., 2014). This could be a result of the very large plasma β in the Jovian magnetotail, which produces plasmoids containing dense plasma and large pressure gradients. The spatiotemporal scales over which these plasmoids, which are also referred to as O-lines, evolve and possibly convert to force-free flux-ropes are also not known. It is not clear which parameter determines the direction and strength of the core field for a plasmoid released in the magnetotail. For externally driven magnetospheres such as Earth’s and Mercury’s, studies have found both strong (Moldwin & Hughes, 1992; Slavin et al., 2003) or weak correlation (Smith, Slavin, Jackman, Poh, et al., 2017) between the IMF orientation and the direction of the core field. In Jupiter’s magnetosphere, the solar wind influence and penetration of the IMF B_Y into the plasma sheet is minimal. However, the ‘bend-back’ of the magnetic field in the magnetodisc introduces a cross-tail magnetic field component in the mid-latitude regions (Khurana et al., 2004).

To understand the role of magnetic reconnection in facilitating mass loss, it is also important to consider alternative theories such as smaller-scale reconnection in the Jovian magnetotail. However, plasmoids observed in the Jovian magnetotail based on the Galileo measurements so far have been large, which could be due to the low temporal cadence of the available instrumentation onboard the Galileo spacecraft. Kronberg, Woch, Krupp, & Lagg, (2008) and Vogt et al., (2014) used data collected by Galileo to study the properties of tailward moving Jovian plasmoids and found their average diameters to between ~9 to 10 R_J and between 2.6 to 20 R_J , respectively. Vogt et al., (2014) inferred the plasmoid size based on the time difference between the two extrema in B_θ during the north-south reversal, whereas Kronberg, Woch, Krupp, & Lagg, (2008) also included the period during which the magnetic field gradually returned to the southward orientation, i.e., the post-plasmoid plasma sheet (PPPS). Kronberg, Woch, Krupp, & Lagg, (2008) observed plasmoid durations to vary between 0 and 50 minutes, with most events having durations between 10 and 20 minutes. They also calculated the plasma flow speeds during the plasmoid events to be between 200 and 1200 km/s. Most plasmoids were associated with flows

156 of around 400 km/s. Similarly, in the Vogt et al., (2014) survey, the 2 to 20 R_J diameters correspond
 157 to an average in-situ duration of 6.8 minutes. The recent survey by (Vogt et al., 2020) used data
 158 collected by the Juno spacecraft to identify signatures of magnetic reconnection and found a similar
 159 result as for the Galileo data.

160 In a previous work, we reported on two Juno-based observations of flux-ropes in the Jovian
 161 magnetotail with diameters comparable to or less than the local ion-inertial length (Sarkango et
 162 al., 2021). This was made possible by the higher resolution magnetometer instrument aboard Juno,
 163 as well as the presence of heavy ions in the magnetosphere which increased plasma length scales.
 164 Our observations extended previous work on magnetic reconnection in the Jovian magnetosphere,
 165 as most plasmoids observed previously by Galileo or Juno were found to have large diameters,
 166 corresponding to in situ signatures lasting several minutes or longer. In contrast, the two events
 167 discussed in Sarkango et al., (2021) had durations of 22 s and 62 s respectively. Under the
 168 assumption that these plasmoids traveled at the Alfvén speed corresponding to that in the lobes,
 169 we had calculated their diameters to be \sim 11,000 and \sim 30,000 km, respectively. Based on these
 170 observations, we hypothesized that magnetic reconnection in the Jovian magnetotail, like other
 171 regions in the space environment, proceeds via the tearing instability in the magnetotail current
 172 sheet. This had also been proposed by Kronberg et al., (2007), who demonstrated that the
 173 magnetotail loading process would take roughly 2 days or more to create conditions conducive for
 174 this instability to occur, which would lead to unloading.

175 In this work, we extend on previous works on plasmoids at Jupiter by conducting a survey
 176 of all possible Jovian plasmoids with in situ signatures shorter than 5 minutes and corresponding
 177 diameters less than \sim 2 R_J . This is achieved by using an automated detection algorithm to identify
 178 plasmoids using transient reversals in B_θ with ‘peak-to-peak’ signatures shorter than 5 minutes
 179 and longer than 10 seconds. By using an empirical density profile and the local Alfvén speed in
 180 the surrounding lobes measured by Juno, we show that the events identified have diameters within
 181 an order of magnitude of the local oxygen ion-inertial length. We also classify plasmoids based on
 182 whether their core-region has magnetic fields that are stronger (flux-ropes) or weaker (O-lines)
 183 than the surrounding magnetic fields in the outer layers of the plasmoid. A force-free flux rope
 184 model is fitted to each flux-rope event, and it is found that out of the 31 plasmoids with strong core
 185 fields, 6 events fit the force-free model well, i.e., they are self-balanced due to internal magnetic
 186 stresses. However, 56 magnetic O-line-type plasmoids were identified and hence were more
 187 commonly observed than flux-ropes. We also use data from the JEDI instrument to show properties
 188 of the energetic electrons and ions during two example plasmoid events. The fluxes of electrons
 189 and ions are larger within these intervals and in the post-plasmoid plasma sheet. For one example,
 190 the electron pitch-angles were isotropic during the interval but field-aligned before and after,
 191 which could be due to betatron acceleration, as has been observed for electron distributions in the
 192 terrestrial magnetotail. Our results highlight that reconnection occurs in Jupiter’s magnetosphere
 193 over a wide range of scales and can accelerate plasma in the process. The frequent observations of
 194 plasmoids with small diameters, which are presumably easier to miss, by a single spacecraft in the
 195 magnetotail also raises questions about the occurrence of ion scale magnetic reconnection in other
 196 regions of the magnetosphere. Nevertheless, our estimates of the total mass carried by ion-inertial
 197 scale plasmoids suggest that they do not directly contribute in a substantial manner to the loss of
 198 mass from the magnetosphere.

199 **2. Data and Methodology**200 **2.1. Juno's Trajectory**

201

202 **Figure 1.** Juno's trajectory in the JSS coordinate system as seen in the equatorial and meridional
 203 projections. Dates and positions corresponding to every fifth apogee are highlighted. Also shown
 204 in panel (a) are the 75% percentile bow-shock (BS) and magnetopause (MP) model by Joy et al.,
 205 (2002).

206 The Juno spacecraft was inserted into an elliptical orbit around Jupiter in June 2016 at
 207 around 06 LT (local time), or close to the dawn meridian. Each subsequent perijove pass was
 208 separated by a time of roughly 53 days. Over the years, Juno naturally precessed towards the
 209 nightside magnetotail, reaching 00 LT (midnight) in early 2020. Simultaneously, its apogee moved
 210 from near-equatorial to mid-latitudes in the southern hemisphere. Over the course of the highly

211 elliptical trajectory (shown in Figure 1), Juno spent a considerable amount of time in the central
 212 plasma sheet, especially during the planet-bound portion of its orbit. During these periods, it
 213 frequently crossed the oscillating magnetotail current sheet, which can be seen in the periodic
 214 reversals of the radial component of the magnetic field (B_r) every 5 hours, or twice every Jovian
 215 rotation period. Juno was most likely to encounter the magnetodisc current sheet at different radial
 216 locations for different local times in the downside magnetotail. Initially (e.g., for years 2016-2018),
 217 when the orbit was less inclined, the current sheet crossings were observed over a broad range of
 218 radial distances, ranging from roughly 30 to 80 R_J . However, the increase in orbital inclination
 219 during the later years (e.g., 2020) meant that current sheet crossings near midnight (00 LT) could
 220 only be observed when the spacecraft was located at lower latitudes where the hinged oscillating
 221 current sheet was expected to occur, i.e., at radial distances nearer to the planet and in the middle
 222 magnetosphere between roughly 20 and 50 R_J . This also had direct implications for the detection
 223 of plasmoid signatures, as magnetic reconnection is also expected to occur close to the current
 224 sheet location, which was not sampled uniformly by Juno.

225 2.2. Data Description

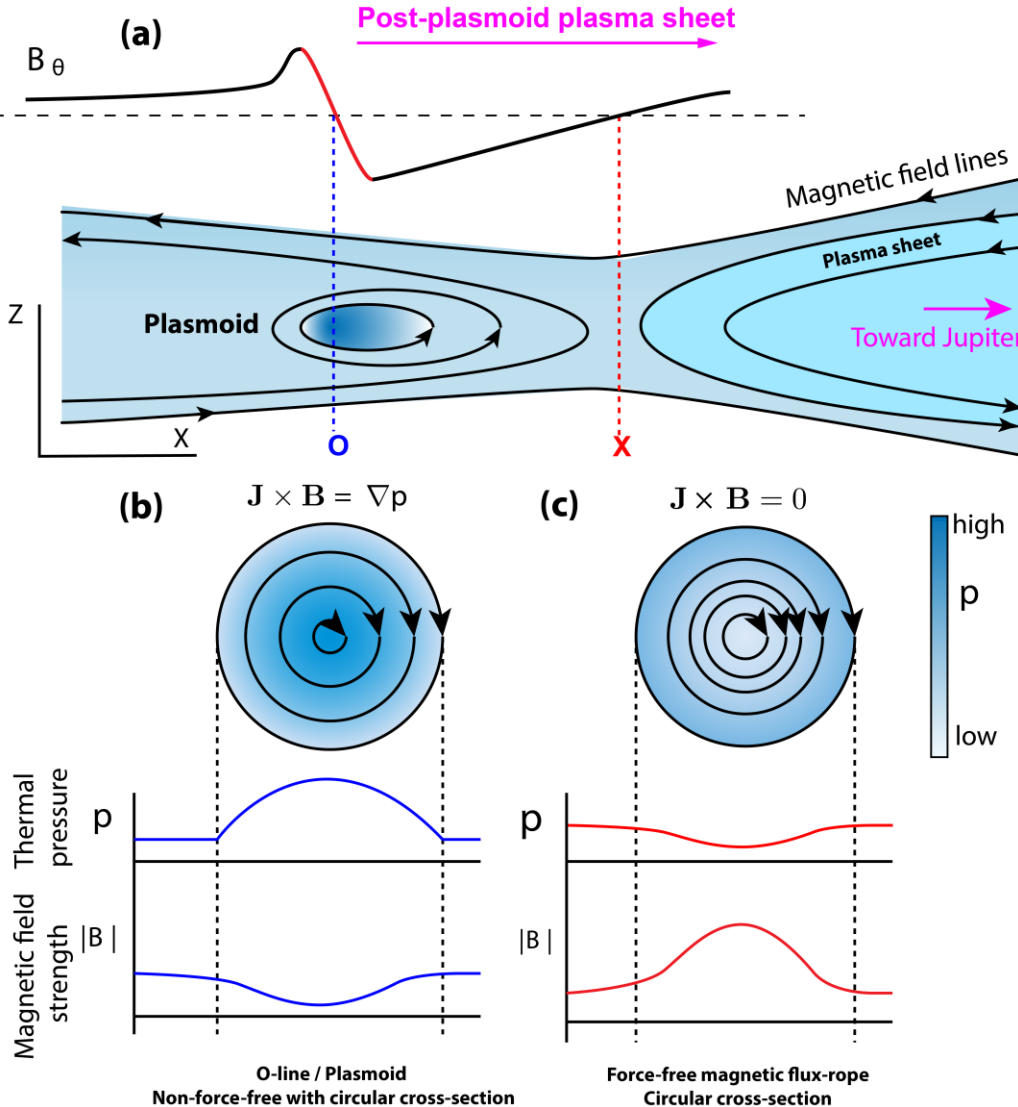
226 In this work, we used 1-s resolution vector magnetic field intensity data collected in situ
 227 by Juno's onboard fluxgate magnetometers (Connerney et al., 2017). We used the magnetometer
 228 data to identify plasmoid signatures on the order of 10 s to 300 s, for which the 1 s cadence was
 229 reasonable as it provides at least 10 magnetic field vectors per event. We also used data from the
 230 Juno Waves instrument (Kurth et al., 2017), which measured the fluctuations in the electric field
 231 between frequencies of 50 Hz and 40 MHz, to identify the low-frequency cutoff for the continuum
 232 radiation and estimate the local electron density (Gurnett et al., 1981; Barnhart et al., 2009). We
 233 supported the fields observations using data from the JEDI energetic particle detectors (Mauk et
 234 al., 2013). Three JEDI instruments were located on the Juno spacecraft; two having a field-of-view
 235 in the spacecraft equatorial plane (JEDI-90 and JEDI-270) and one looking perpendicular to the
 236 spacecraft equatorial plane (JEDI-180). JEDI could measure electrons in the energy range between
 237 18 keV to 740 keV. JEDI could also measure and distinguish between ion species based on the
 238 time-of-flight channels, specifically protons (\sim 37 keV – 2 MeV), oxygen (\sim 130 keV – 10 MeV)
 239 and sulfur (\sim 130 keV – 11 MeV) ions. In favorable conditions, the rotation of Juno about its spin
 240 axis allowed for near-complete pitch-angle coverage with a typical collection time of 30 s.
 241 However, for most times when Juno was in the middle and outer magnetosphere, the JEDI
 242 instruments were operating at a lower data rate mode with reduced energy resolution to facilitate
 243 data transfer during these periods.

244 2.3. Magnetic signatures of plasmoids

245 We used the Juno data to search for plasmoids in the Jovian magnetotail by identifying
 246 reversals in the north-south component of the magnetic field, i.e., B_z or B_θ in Cartesian JSS or
 247 spherical JSS coordinate systems respectively. An illustration of the expected magnetic signature
 248 of a tailward moving plasmoid containing helical magnetic fields is illustrated in Figure 2 (a).

249 The sense of the B_z reversal, i.e., from north-to-south or vice-versa, can be used to infer
 250 the direction of travel of the plasmoid. Observations in the terrestrial magnetosphere have shown
 251 that plasmoids which travel tailward usually correspond to a B_z reversal from positive to negative
 252 values (Slavin et al., 2003). While the Earth's magnetic moment points predominantly southward,
 253 Jupiter's internal magnetic moment points northward. This implies that tailward moving plasmoids

254 in the Jovian magnetotail would have the opposite sense of reversal as seen at Earth, i.e., B_z would
 255 change from negative to positive values (assuming that a single plasmoid is released). On the other hand,
 256 planetward moving plasmoids would result in B_z changing from positive to negative values.



257

258 **Figure 2.** (a) Magnetic signature and representative geometry of a tailward moving plasmoid
 259 with a post-plasmoid plasma sheet. (b-c) Schematics showing the different magnetic field and
 260 thermal pressure profiles of magnetic O-lines (b) and force-free flux-ropes (c) with circular
 261 cross-sections.

262 To prevent ambiguity due to the oscillating Jovian current sheet and magnetodisc, analysis
 263 of magnetic field components in the Jovian system was conducted in the spherical JSS coordinate
 264 system where B_r , B_θ and B_ϕ represented the radial, co-latitudinal and azimuthal components of
 265 the magnetic field. In this system, the periodic motion of the current sheet is largely limited to the
 266 radial and azimuthal components (B_r and B_ϕ), which are anti-correlated due to the bend-back
 267 phenomena (Khurana et al., 2004). In a quiet time magnetotail and in the absence of reconnection,
 268 B_θ is predominantly positive (In our work, like the previous studies, positive B_θ corresponds to

negative B_z at the equator). Hence, the magnetic signature of a tailward moving plasmoid would be a positive-to-negative reversal in B_θ , and opposite (negative-to-positive) for a planetward moving plasmoid (Figure 2). Additionally, plasmoids may or may not possess a core field inside the outer helical magnetic structures (flux-ropes), which can be seen predominantly in the azimuthal or radial components (B_ϕ or B_r) or as a localized increase in the magnetic field strength within the interval corresponding to the reversal of B_θ (Figure 2 (c)).

2.4. Minimum Variance Analysis

We used the magnetic field based minimum variance analysis (referred to as MVA or BMVA in the literature) to characterize the helical magnetic structure. A local cartesian coordinate system was determined, whose orthogonal directions represent the directions of maximum, intermediate and minimum variance of the magnetic field during the plasmoid interval. This was done by first constructing the variance matrix M according to the following equation (Sonnerup & Cahill, 1967),

$$M_{ij} = \langle B_i B_j \rangle - \langle B_i \rangle \langle B_j \rangle, \text{ for } i, j \in \{x, y, z\} \quad (1)$$

The eigenvectors of the variance matrix corresponding to the decreasing magnitude of the eigenvalues (λ_L , λ_M , λ_N) provided the directions of maximum (\vec{x}_L), intermediate (\vec{x}_M) and minimum variance (\vec{x}_N).

For plasmoid signatures in the magnetotail, the magnetic field varies most in the north-south (Z or θ) direction. The maximally varying component (B_L) also reverses sign. In the case of a flux-rope, the local increase in the core field direction can be seen in the component of intermediate variance (B_M). This leads to a near elliptical path when visualized as a hodogram of the B_L and B_M components, also referred to as a rotation (Slavin et al., 1989).

MVA fails to determine the orientation of the variance directions if two or more eigenvalues of the variance matrix are similar in magnitude. In other words, there are times when the variance coordinate system is *degenerate*. This is verified in the present work by requiring that the ratio of larger to smaller eigenvalues be greater than 3. Additionally, we also imposed the condition by Rosa Oliveira et al., (2020) using the metric P (shown below), where $P > 4.5$ considered to be sufficient to validate the MVA eigensystem.

$$P = \frac{100}{\lambda_L^{1.5}} \times (\sqrt{\lambda_L} - \sqrt{\lambda_M})(\sqrt{\lambda_L} - \sqrt{\lambda_N})(\sqrt{\lambda_M} - \sqrt{\lambda_N}) \quad (2)$$

2.5. Force-free Flux-rope Modeling

Plasmoids with strong axial core fields are referred to as ‘flux-ropes’. A subset of flux-ropes within which pressure gradients are negligible and which are in force equilibrium due to the self-balancing magnetic forces are termed ‘force-free’ (Kivelson & Khurana, 1995). The expected pressure and magnetic field profile within O-line type plasmoids and magnetic flux ropes is shown in Figure 2. In the O-line type plasmoids, the magnetic pressure of the helical wraps is balanced by the thermal pressure gradient. One solution for axially symmetric force-free flux-ropes with circular cross-sections takes the following form (Lepping et al., 1990; Slavin et al., 2003),

308 $B_A = B_0 J_0(\alpha r)$ (3)
 309

310 $B_T = B_0 H J_1(\alpha r)$ (4)
 311

312 Where B_A and B_T are the axial and tangential components of the magnetic field, H is the
 313 handedness (either 1 or -1), J_0 and J_1 are the Bessel functions of the first kind, α is a constant
 314 parameter and r here refers to the ratio between the impact parameter, which is the distance from
 315 the center of the flux-rope at closest approach, and the radius of the flux-rope. In this work, $\alpha =$
 316 2.4048 was chosen as it results in the tangential field component being zero when $r = 1$ (at the
 317 flux-rope edge).

318 For a given interval exhibiting a flux-rope-like signature, we used Eq. 3-4 to fit a constant-
 319 α flux-rope to the observations to determine whether the helical structures seen in the data were
 320 force-free. This was achieved by varying B_0 , r , H and the spherical angles providing the axial
 321 orientation of the flux-rope, θ_A and ϕ_A , such that the Chi-squared error between the observations
 322 and the force-free model was minimized (Lepping et al., 1990).

323
$$\chi_r^2 = \frac{1}{N} \sum_{i=1}^N \left[(B_x - B_{x,m})^2 + (B_y - B_{y,m})^2 + (B_z - B_{z,m})^2 \right]$$

 324 (5)

325 This was achieved in two steps using an open-source nonlinear least-squares fitting
 326 package (Newville et al., 2016). Firstly, the magnetic field components were normalized by the
 327 local magnetic field strength within the interval. Next, the flux-rope model was fitted to the
 328 observations for all parameters except for B_0 . The initial values for θ_A and ϕ_A , i.e., the flux-rope
 329 orientation, were chosen based on the eigenvector for intermediate variance ($\overrightarrow{x_M}$) as provided by
 330 the minimum-variance analysis. Then the minimization was repeated, keeping all parameters fixed
 331 to their optimized values, but varying B_0 to scale the modeled flux-rope's core field.

332 2.6. Automated detection of plasmoids

333 We used an automated algorithm to detect possible plasmoid signatures in the magnetic
 334 field observations made by the Juno magnetometer. For identifying potential signatures, we used
 335 a method like that used by Smith, Slavin, Jackman, Fear, et al., (2017) for the Kronian magnetotail
 336 and by Vogt et al., (2014) for the Jovian magnetotail. Firstly, within an interval in the 1-s resolution
 337 magnetometer data, all times corresponding to a reversal in B_θ , either from positive-to-negative or
 338 vice-versa, were identified. Reversals which occurred beyond 05 LT on the dawnside and beyond
 339 90 R_J in radial distance from the planet were discarded to prevent contamination due to proximity
 340 to the magnetopause, where the magnetic field is highly variable.

341 Next, for each reversal, the times corresponding to the extrema in B_θ for the event were
 342 identified. As there can be multiple local maxima and minima in the B_θ magnetic field
 343 observations, we adopted the method used by Smith, Slavin, Jackman, Fear, et al., (2017) and
 344 identified maxima-minima (or vice-versa) pairs within a period of +/- 10 min from the B_θ reversal.
 345 Pairs in which the peak-to-peak B_θ extrema were less than 2 nT or the standard deviation of the
 346 B_θ component during a 100 min interval centered on the reversal in question were considered

347 inconclusive and discarded. Pairs in which the excursion into negative B_θ values was a factor of 6
 348 smaller than that in the positive direction (and vice-versa) were also discarded. Additionally, only
 349 those extrema pairs were considered whose start and end times were separated by a duration of at
 350 least 10 s and at most 5 min, which form the lower and upper limit for the events identified in this
 351 study. The lower limit was chosen such that there are at least 10 vector measurements for
 352 subsequent analysis. As the purpose of this work was to study small-scale plasmoid events, we
 353 limited the algorithm to signatures lasting less than 5 min. The range in the present work overlaps
 354 with the lower bins of a previous survey by Vogt et al., (2014) of plasmoids identified by the
 355 Galileo magnetometer.

356 For each of the remaining pairs of extrema, which correspond to potential start and stop
 357 times for a plasmoid event, a linear function was fitted to the B_θ observations (Smith, Slavin,
 358 Jackman, Fear, et al., 2017). Those extrema pairs which showed low degree of correlation with the
 359 observations (quantified by the coefficient of determination $r^2 < 0.85$) were discarded.

360 Next, additional filters were applied based on the minimum-variance analysis, which was
 361 conducted on all remaining extrema pairs. Events in which the eigenvector corresponding to the
 362 direction of maximum variance did not have a predominantly Z_{JSS} component ($\hat{x}_L \cdot \hat{z} < 0.8$) were
 363 discarded. Pairs for which the ratio of the maximum to intermediate and intermediate to minimum
 364 eigenvalues were less than 3, or for which the P value was less than 4.5, were also removed from
 365 consideration. Lastly, to only capture plasmoid events close to a magnetotail current sheet crossing
 366 and prevent identification of traveling compression regions (TCRs) in the magnetotail lobes
 367 (which was outside the scope of the present work), additional filters were applied to limit the
 368 detection to events in which the minimally varying component of the magnetic field (B_N) as well
 369 as the radial component in the JSS spherical coordinate system (B_r), were less than 2 nT.

370 Of the remaining extrema pairs, the pair which fits best the B_θ observations using a linear
 371 function was identified (i.e., highest r^2) and chosen to be the start and end time for that event. In
 372 this procedure to detect B_θ reversals no distinction was made between positive-to-negative or
 373 negative-to-positive sense, as both tailward and planetward moving plasmoids (respectively) are
 374 likely to occur in the magnetotail. The conservative approach used by this algorithm ensured good
 375 candidates for plasmoids in the Jovian magnetotail. The procedure was repeated for each B_θ
 376 reversals detected by Juno, though only 87 reversals passed all criteria.

377 3. Results

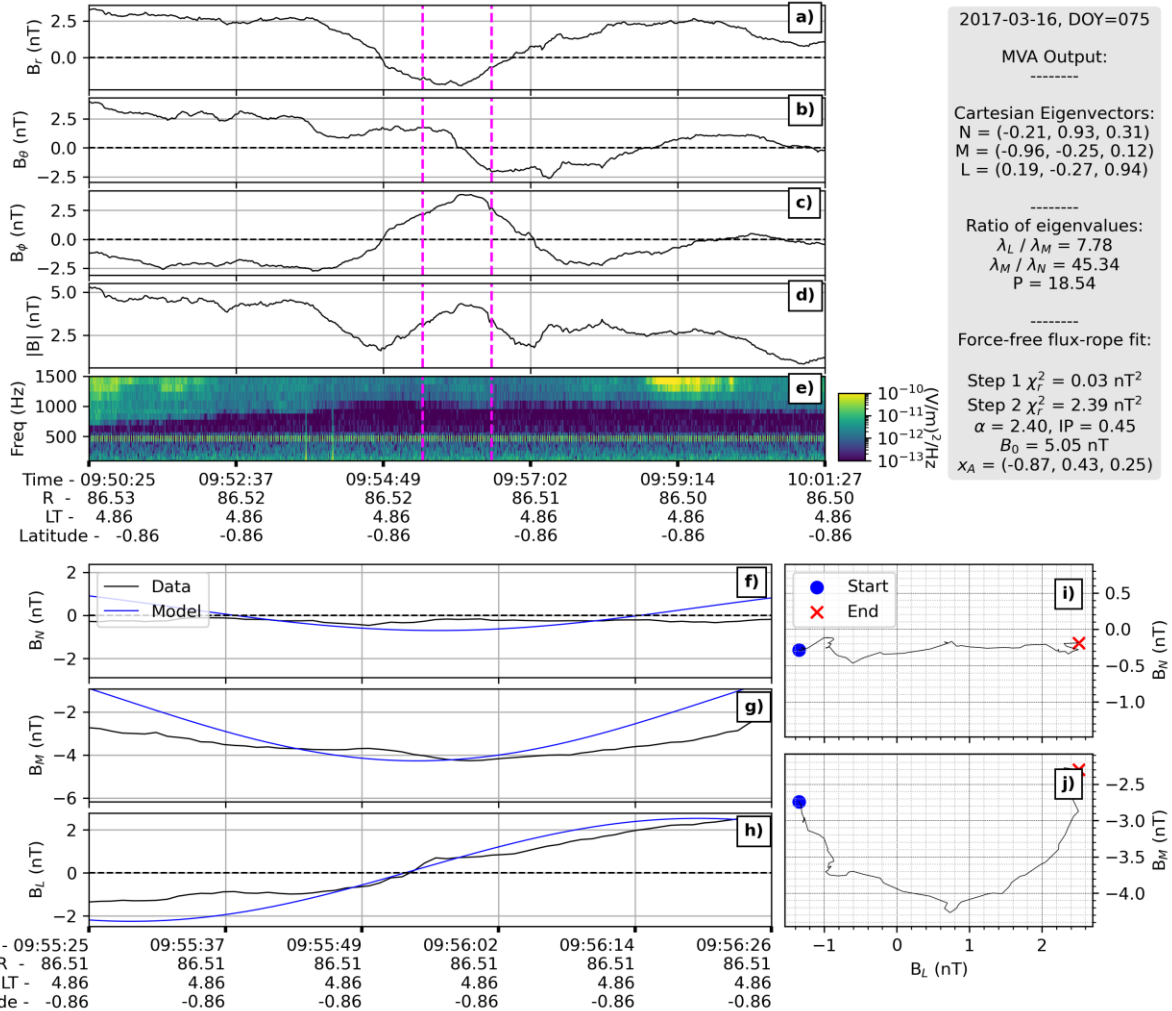
378 3.1. Case Studies: Magnetic field and energetic particle signatures of plasmoids

379 In this section we discuss the magnetic field and energetic particle signatures of two
 380 examples of ion-inertial scale plasmoids identified by our automated algorithm.

381 3.1.1. Example 1: Flux-rope - DOY 76, 2017

382 In Figure 3 (a)-(d) we show the magnetic field data in the spherical JSS coordinate system
 383 for a plasmoid event occurring on DOY 75 in 2017 roughly between 09:55:25 and 09:56:26 UTC.
 384 Juno was in the dawnside magnetotail near ~ 05 LT at ~ 86.5 R_J from Jupiter. This interval was
 385 close to a current sheet crossing, as can be seen in the smooth reversals in the radial (B_r) and
 386 azimuthal (B_ϕ) components from positive to negative values, or vice-versa. The southward-to-

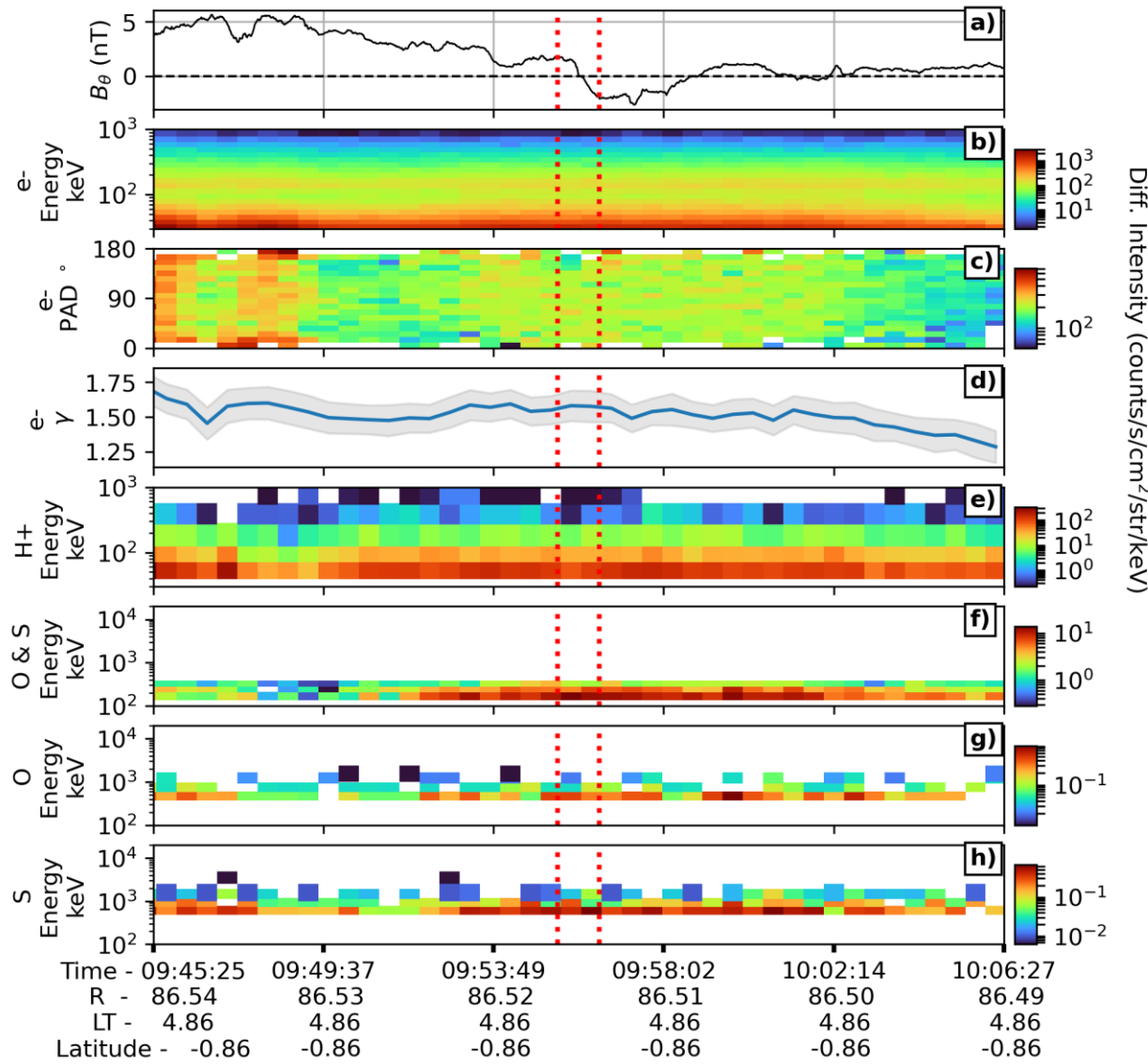
387 northward B_θ reversal is accompanied by an interval of negative B_θ . The sense of the reversal
 388 suggests that the plasmoid was moving tailward with respect to Juno.



389
 390 **Figure 3.** Magnetic field observations of a magnetic flux-rope event on DOY 75, 2017 by the
 391 Juno spacecraft in the dawnside magnetotail. Panels (a)-(d) show the magnetic field intensity in
 392 the spherical JSS coordinate system. The Waves electric field spectra is shown in Panel (e).
 393 Panels (f)-(g) show the components of the magnetic field in the minimum-variance coordinate
 394 system corresponding to the minimum, intermediate and maximum eigenvector. The magnetic
 395 signature of the best-fit modeled force-free flux-rope is shown in blue. Panels (h)-(i) show the
 396 hodograms between the field components in the MVA coordinates. Details of the minimum
 397 variance analysis and the force-free flux-rope modeling are shown in the grey box.

398 Results of the MVA and force-free modeling for this interval are shown in Figure 3 (f)-(j),
 399 where the magnetic field components are plotted in the variance coordinate system. The minimally
 400 varying component (B_N) was predominantly in the X_{JSS} direction with values less than 0.3 nT,
 401 compared to the field strength between 2 and 4 nT. A reversal could be seen in the maximally
 402 varying component (B_L) which was accompanied by a moderate increase in the intermediate
 403 component (B_M) near the center of the interval, which can also be visualized as a rotation in the
 404 $B_L - B_M$ hodogram (Figure 3 (j)). This transient increase in the core field was also seen in the
 405 magnetic field magnitude and we classified this event as a magnetic flux rope. The ratios of the

406 eigenvalues of the variance matrix were 7.78 and 45.34, which were large enough to suggest that
 407 the MVA analysis unambiguously determined the variance coordinate system. Also shown in
 408 Figure 3 (f)-(j) is the modeled force-free flux rope (in blue) which results in the least χ^2_r . The
 409 reduced Chi-squared error between the data and the modeled flux-rope was large ($\sim 2.39 \text{ nT}^2$)
 410 compared to the mean field strength ($\sim 4 \text{ nT}$), which indicated that the observed flux-rope was not
 411 force-free. Nevertheless, the increase in the magnetic field strength and the intermediate
 412 component show that this event is a magnetic flux-rope with a strong axial core field.



2017-03-16, DOY=075

413
 414 **Figure 4.** Energetic particle observations made by the JEDI instruments on board the Juno
 415 spacecraft for the same event as shown in Figure 4. Panel a) shows the variation of B_θ during the
 416 event for context. Each consecutive panel shows (b-c) the dynamic energy and pitch-angle
 417 spectra for the electrons, (d) the omnidirectional energy spectral index γ for the electrons, the

418 energy spectra for (e) protons, (f) indistinguishable sulfur and oxygen ions O/S, (g) oxygen ions,
 419 and (h) sulfur ions. All spectra have units of differential intensity i.e., counts/s/str/cm²/keV.

420 Figure 3 (e) shows the dynamic spectra for the high-frequency fluctuations in the electric
 421 field as measured by the Juno Waves instrument. The continuum radiation was observed
 422 throughout the interval with a low-frequency cut-off at roughly 1000 Hz. Assuming this to be the
 423 electron plasma frequency, we estimated the local electron density during this interval to be ~0.012
 424 cm⁻³. Assuming quasi-neutrality and a singly charged ion mass of 16 amu, this density corresponds
 425 to an ion inertial length of 8178.15 km.

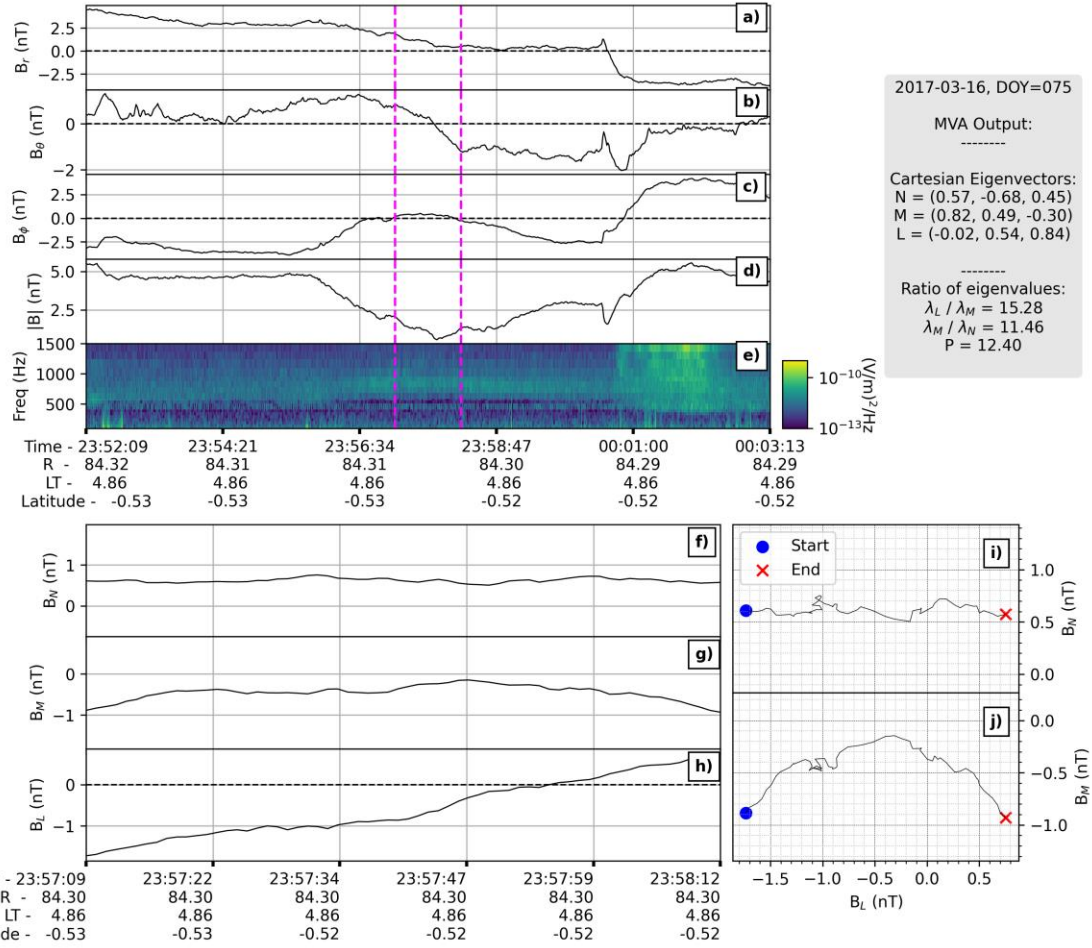
426 In Figure 4 we show the differential intensity measurements by the JEDI energetic particle
 427 detector for the same event as shown in Figure 3 for the electrons, protons, oxygen, and sulfur
 428 ions, averaged in bins of 30 s each. We show the energy and pitch-angle spectra for the electrons
 429 (b)-(c) since higher resolution electron data was available. Also shown for the electrons in (d) is
 430 the energy spectral index (γ) obtained by fitting the relation $I = I_0(E/E_0)^{-\gamma}$ to the omnidirectional
 431 differential intensities (I). Only the energy dynamic spectra are shown for the ions (e)-(h), and
 432 their data was limited due to the lesser energy channels and pitch-angle coverage. JEDI was unable
 433 to distinguish between the heavy ions at relatively low energies and these are shown together in
 434 panel (f). The JEDI data shown in this figure was resampled to a cadence of 30 s using data from
 435 all operating JEDI detectors. There was a moderate increase in the electron flux near the plasmoid
 436 event. The electron spectral index decreased after the passage of the plasmoid. Ion fluxes also
 437 increased near the plasmoid. The increase in ion flux is most prominent for the sulfur and low
 438 energy S/O ions.

439 **3.1.2. Example 2: O-line - DOY 75, 2017**

440 Juno observed another plasmoid event between 23:57:08 and 23:58:12 UTC on DOY 75,
 441 2017. The magnetic field and Waves spectra for this example are shown in Figure 5. The magnetic
 442 field reversed from a southward to northward configuration before and after this event (B_θ changed
 443 from positive to negative) and there was no increase seen in the radial or azimuthal component
 444 within the reversal. This plasmoid did not have a core field signature and had its minimum field
 445 strength at the center of the interval and was therefore classified as a magnetic O-line. The
 446 minimum variance analysis showed a similar result, with a minimum in the intermediate variance
 447 component near the center of the interval. The core field direction, as inferred based on the
 448 direction of minimum variance for O-lines, was skewed in the XY plane with a large out-of-plane
 449 component. The ratios of the eigenvalues were very large ($\lambda_L/\lambda_M = 15.28$ and $\lambda_M/\lambda_N = 11.46$)
 450 indicating that the MVA coordinate system was well defined. As this event did not have a core
 451 field, no attempt was made to fit a force-free flux-rope. The Waves spectra, shown in panel (e)
 452 showed that the cutoff for the continuum radiation briefly increased during the plasmoid interval
 453 from ~500 Hz to 700 Hz. If the cutoff occurs at the electron plasma frequency, this transient
 454 increase indicated that the electron density also increased within the interval. This is consistent
 455 with the low magnetic field in the center for the O-line type plasmoid. The ~700 Hz cutoff
 456 frequency corresponds to an electron density close to 0.006 cm⁻³ and an ion inertial length of
 457 ~11683 km assuming quasi-neutrality and a singly charged oxygen ion.

458 Data from the JEDI detectors for this interval is shown in Figure 6. A moderate increase in
 459 the electron flux was seen during the plasmoid interval (b). On the other hand, proton, oxygen and
 460 sulfur fluxes increased by almost two orders of magnitude compared to times before the plasmoid
 461 event (e)-(h). The large ion fluxes were seen consistently even after the B_θ reversal and during the

462 prolonged interval of negative B_θ , or the post-plasmoid plasma sheet. Increases in particle fluxes
 463 were also seen in data collected by the Galileo EPD (Kronberg et al., 2005) for the larger plasmoids
 464 discussed in previous surveys.

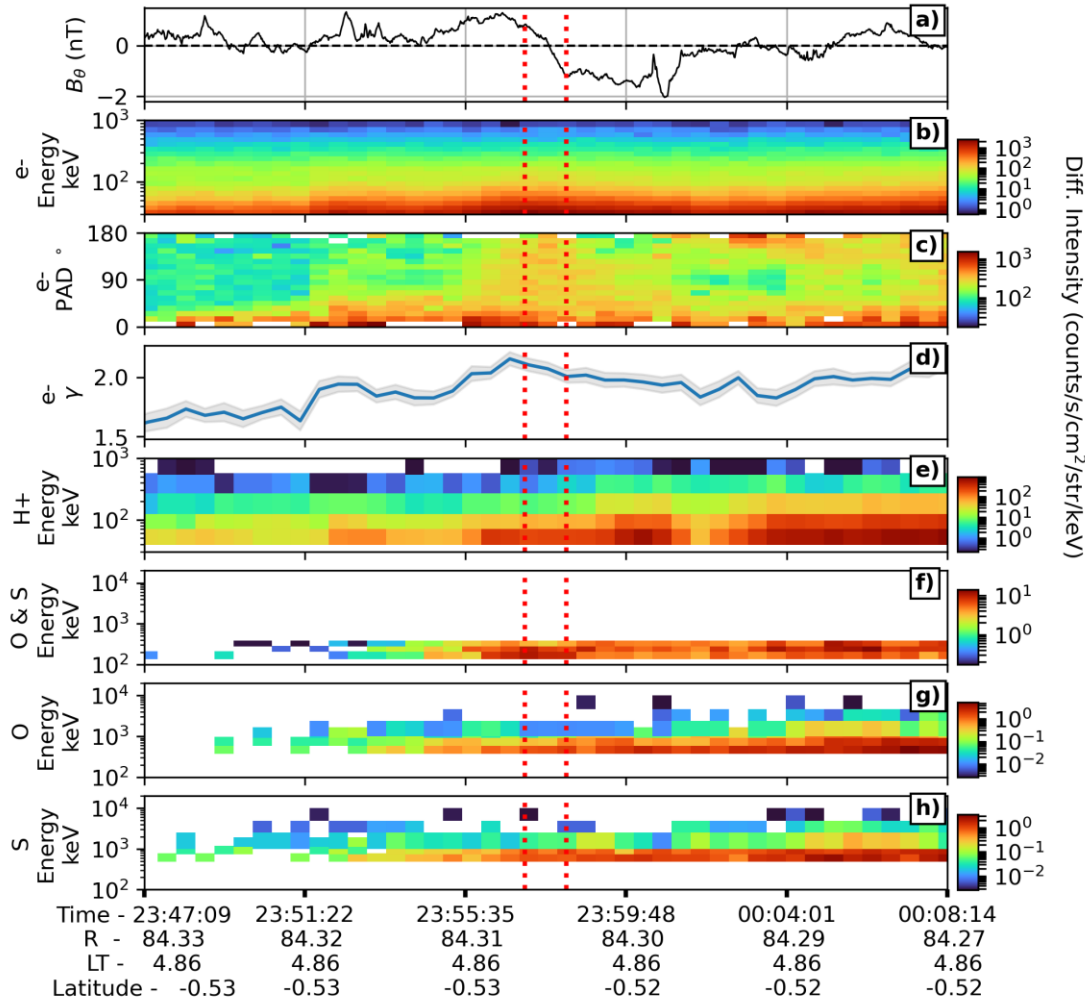


465

466 **Figure 5.** Magnetic field signatures (a)-(d) and electric field spectra (e) obtained by the Juno
 467 magnetometer and Waves instruments for a plasmoid event on DOY 75, 2017 in a similar format
 468 as Figure 3. No force-free flux rope was fitted for this interval as the field is weakest in the
 469 interior of the plasmoid and it is classified as a magnetic O-line.

470 There was near-complete pitch-angle coverage for the electrons, which were
 471 predominantly field-aligned before and after the plasmoid. Before the event, electrons were seen
 472 streaming mainly along the magnetic field. The distribution gradually became more isotropic near
 473 the plasmoid interval and gradually returned to being field aligned after the passage of the
 474 plasmoid, from 23:58 DOY 75 to ~02:00 DOY 76. It has been demonstrated that electron
 475 distributions near flux-ropes are influenced by the Fermi and betatron acceleration processes
 476 (Zhong et al., 2020; Vaivads et al., 2021) and it is plausible that similar processes are occurring in
 477 the present situation. The observed pitch-angle dispersion is seen primarily for electrons with
 478 pitch-angles less than 90°, which could also be because of the abundance of field-aligned electrons
 479 before and during this interval. Field-aligned and anti-field-aligned electrons are observed in the
 480 post-plasmoid plasma sheet (e.g., at DOY 76, 00:02). The electron spectral index γ , shown in

481 Figure 6 (d), increased until the plasmoid encounter and decreased gradually within the PPPS, i.e.,
 482 the electron spectra ‘hardened’ in the reconnection exhaust.



2017-03-16, DOY=075, 076

483

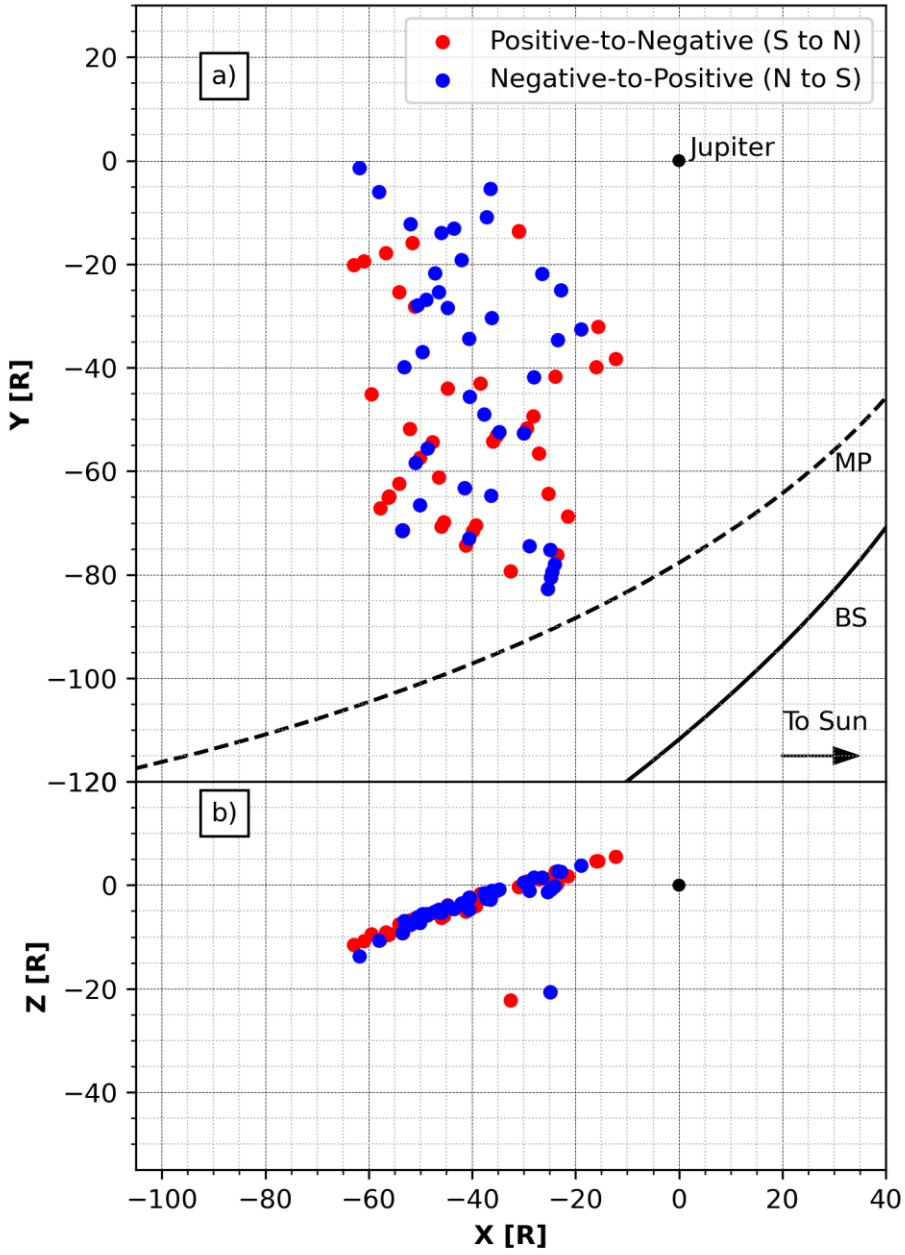
484 **Figure 6.** Energetic particle differential intensities measured by the JEDI instruments for the
 485 event shown in Figure 5 in a similar format as for Figure 4.

486 In Example 2, the magnetic field was predominantly southward before the event (positive
 487 B_θ) and was in a northward configuration (negative B_θ) for a brief period (>3 minutes) after. The
 488 gradual return to positive B_θ is consistent with the presence of a large post-plasmoid plasma sheet
 489 (PPPS). This is further supported by JEDI observations of higher ion fluxes lasting for the entire
 490 PPPS duration. This interpretation follows the schematic shown in Figure 2 (a) for a tailward
 491 moving plasmoid with a PPPS.

492 JEDI data for the electrons and ions was available at high cadence for the two examples
 493 discussed above. However, this was not the case for most events in our survey. For this reason,
 494 subsequent analysis of the plasmoids uses data gathered primarily by the Juno magnetometer and
 495 Waves instruments.

496

3.2. Survey results: Location and sense of magnetic field reversals



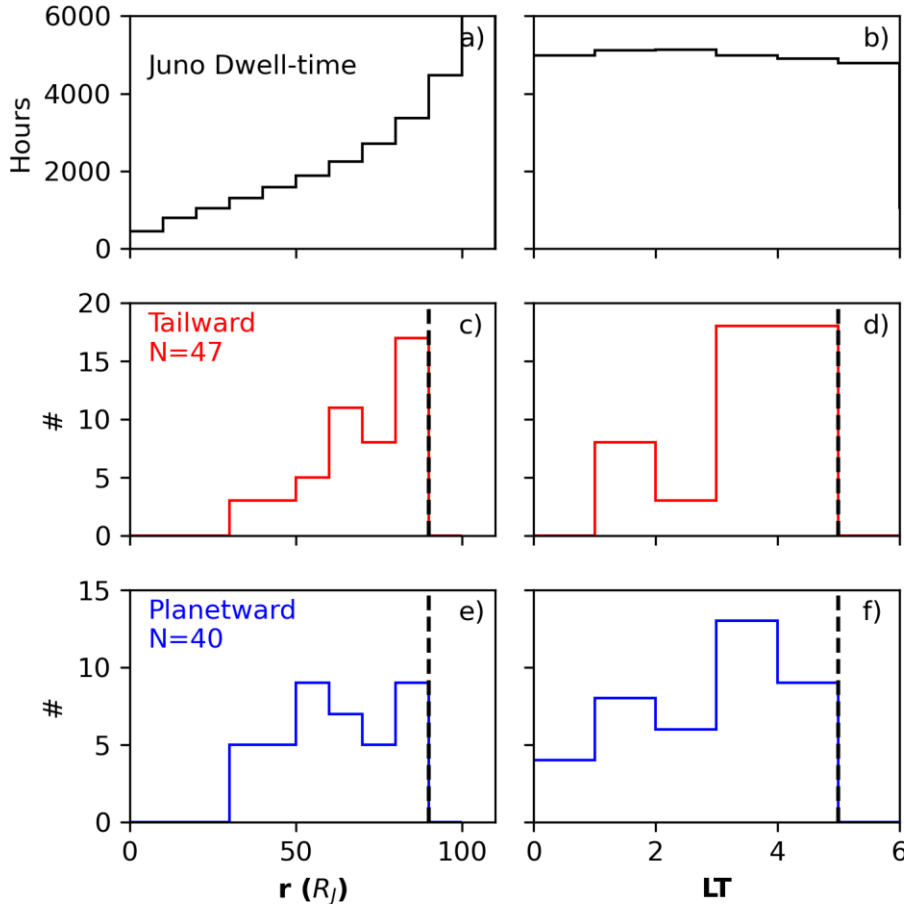
497

498 **Figure 7.** Locations of the plasmoid events in the JSS coordinate system identified by our
499 automated algorithm, colored according to the sense of reversal in B_θ .

500 The automated algorithm searched for plasmoid signatures between DOY 49, 2017 and
501 DOY 150, 2020. Although Juno was inserted into orbit in June 2016, earlier times were effectively
502 not considered due to the $LT < 5$ filter used in the algorithm to prevent misidentification due to the
503 magnetic field fluctuations near the magnetopause. In this period, corresponding to the stringent
504 criteria described in Section 2.6, the algorithm detected 87 plasmoids with peak-to-peak durations
505 less than 5 minutes. The list of the detected plasmoids is given in the Supporting Information. Out
506 of the 87 events, 47 corresponded to a positive-to-negative reversal in B_θ and were thus likely

507 tailward-moving plasmoids, while the remaining 40 events corresponded to a negative-to-positive
 508 reversal in B_θ and were planetward-moving plasmoids. The terms ‘tailward’ and ‘planetward’ are
 509 used interchangeably in this work with south-to-north and north-to-south reversals of the magnetic
 510 field, respectively, though this is strictly applicable only in the case of a single plasmoid.

511 The locations of the 87 events identified by the algorithm are shown in Figure 7. The vast
 512 majority ($N=86$) of events were identified in the planet-bound portion of Juno’s orbit, which lies
 513 within the volume of the expected oscillating magnetotail current sheet. All events were located
 514 roughly between 23 and 05 LT due to Juno’s orbit being in the midnight to dawn quadrant of the
 515 magnetotail between years 2016 and 2020.



516

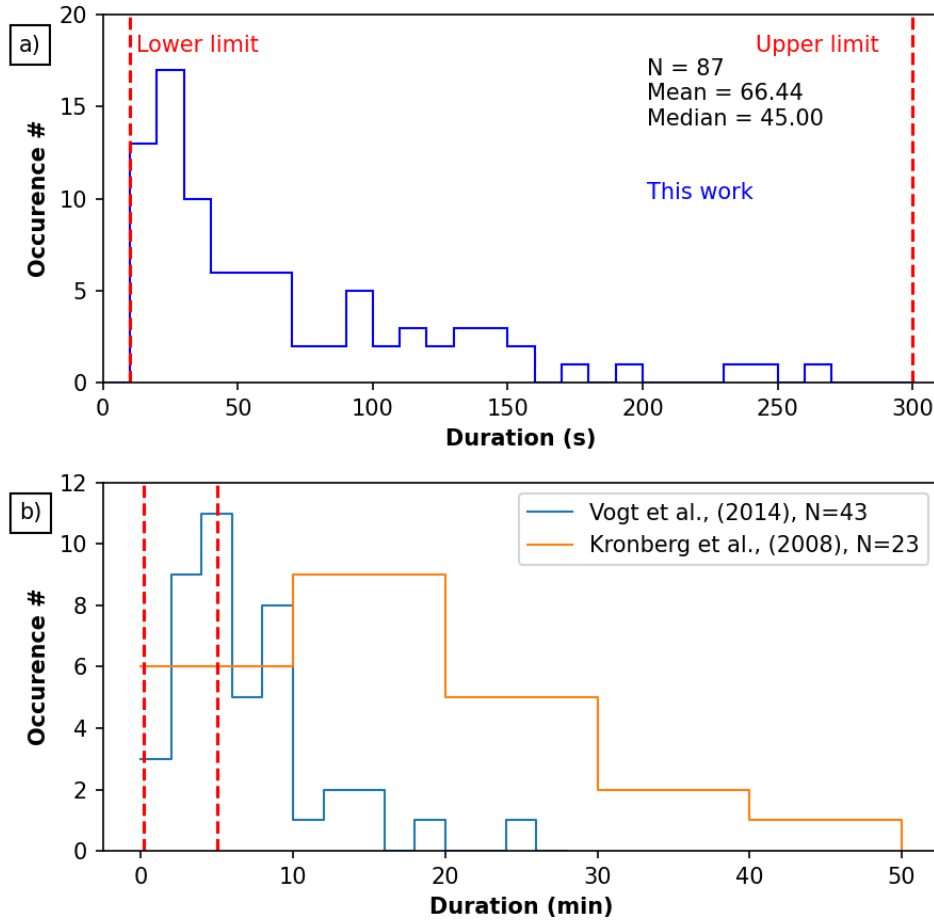
517 **Figure 8.** Histograms showing Juno’s dwell time in hours in different radial and local time bins
 518 (a-b), as well as the number of tailward moving (c-d) and planetward-moving (e-f) plasmoids
 519 identified by the algorithm in the different bins. The dashed line marks the limits of the detection
 520 algorithm. Here, ‘tailward’ and ‘planetward’ refers to the motion expected for a single plasmoid
 521 based on the sense of the B_θ reversal.

522 In Figure 8 we show using histograms the time spent by Juno in different radial and local
 523 time regions (a)-(b). Due to Juno’s elliptical orbit, it spent more time in the outer magnetosphere
 524 as it slowed down near its apogee. On the other hand, each local time between 00 and 06 was
 525 sampled almost equally. In panels (c)-(d) we show the occurrence of the planetward-moving
 526 plasmoids different radial and local bins. The 47 tailward moving plasmoids were identified

527 between 30 and 90 R_J (the latter being specified by the automated algorithm). In general, tailward
 528 events were observed more frequently at larger radial distances, with the most events ($N=18$) being
 529 observed between 80 and 90 R_J . In terms of local time, >38 tailward events were seen between 03
 530 and 05 LT, or close to the downside flank. The distribution for planetward moving plasmoids
 531 ($N=40$) was not skewed towards larger radial distances like for the tailward events, though out of
 532 a total of 40, 30 events were seen at distances beyond 50 R_J . Although they were observed at all
 533 local times, the maximum number of planetward events ($N=13$) were seen between 03 and 04 LT.
 534 4 planetward plasmoids were also seen between 00 and 02 LT, or close to midnight.

535 In interpreting Figure 8, we note again that Juno's trajectory and increasing inclination with
 536 time implied that current sheet crossings, and thus, small-scale plasmoids which occur close to the
 537 current sheet, were more likely to be seen for the earlier years (2017-2019 or between 03-05 LT)
 538 at larger radial distances, and for the later years (2019-2020 or between 00-03 LT) at smaller radial
 539 distances closer to the planet, respectively (see Figure 1).

540 3.3. Duration and size of plasmoids

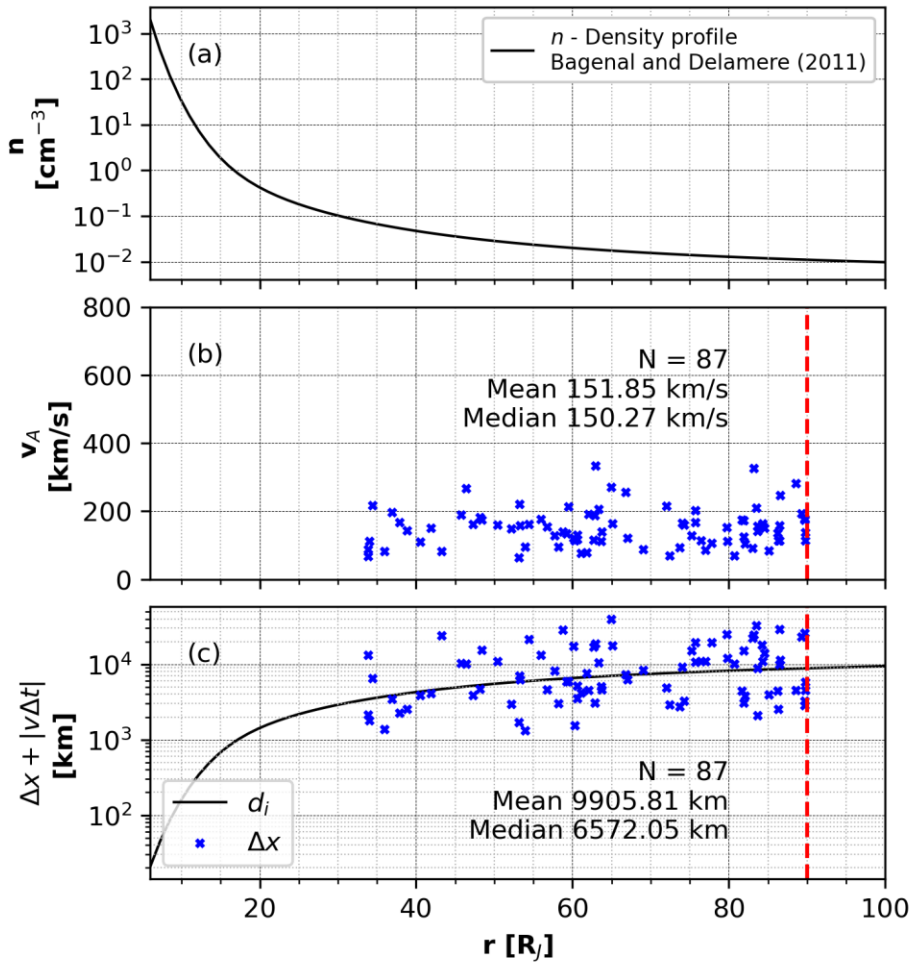


541

542 **Figure 9.** Histogram showing the “peak-to-peak” durations of the identified plasmoids in the
 543 present study (a) based on the Juno data and by Vogt et al., (2014) and Kronberg et al. (2008)

544 using data from the Galileo magnetometer (b). The lower and upper limits specified in our
 545 identification algorithm are highlighted using red dashed lines.

546 In Figure 9 (a) we show a histogram of the peak-to-peak durations of the 87 plasmoids
 547 identified by the algorithm. The minimum and maximum allowed event size were specified to be
 548 10 s and 300 s respectively, as in this work we focus only on small-scale plasmoids with potential
 549 diameters comparable to the ion-inertial length. A majority (N=50) of the identified plasmoid
 550 events had durations less than 60 s. In general, plasmoids with shorter-duration in situ signatures
 551 (and hence smaller diameters), were observed more frequently than plasmoids with longer-
 552 duration in situ signatures. The mean and median durations for the small-scale plasmoids were
 553 found to be 66.44 s and 45 s, respectively. Small-scale events were most likely to be seen having
 554 signatures lasting between 10 and 30 s, with 30 out of the 87 events in these two bins. For
 555 comparison, the histogram of plasmoid durations by the Vogt et al., (2014) and Kronberg, Woch,
 556 Krupp, & Lagg, (2008) surveys are shown in Figure 9 (b), with dashed lines showing the event
 557 selection thresholds used by our algorithm. Vogt et al., (2014) found that plasmoids were most
 558 likely to have signatures lasting for 5 minutes, with a decreasing trend toward the 0-2 min and 2-
 559 4 min bins. (Kronberg, Woch, Krupp, & Lagg, 2008) use a different definition for the plasmoid
 560 duration, however, they found a similar result with the distribution being skewed towards smaller
 561 durations which were less than 20 min.



562

563 **Figure 10.** a) The Bagenal and Delamere (2011) density profile as a function of radial distance.
 564 b) The average magnetotail lobe Alfvén speed +/- 5 min from the corresponding B_θ reversal for
 565 each plasmoid event. c) Scatter plot showing the diameters of the identified events, calculated by
 566 assuming that the plasmoids travel at the lobe Alfvén speed shown in panel b. The solid line
 567 shows the expected ion-inertial length calculated using the Bagenal and Delamere (2011) density
 568 profile and using an ion mass of 16 amu. The dashed line marks the limit of the detection
 569 algorithm.

570 We estimated the diameters of the identified plasmoids by assuming that they were
 571 travelling at the Alfvén speed in the magnetotail lobes, which we estimated based on the measured
 572 in situ magnetic field strength and an empirical density profile (Bagenal & Delamere, 2011).
 573 Figure 10 shows the typical Alfvén speeds for each event (b) along with the empirical density
 574 profile used (a)-(b). The Alfvén speed was calculated by averaging the magnetic field strength
 575 during an interval +/- 5 min from the reversal in B_θ . The mean and median Alfvén speeds
 576 calculated in this manner was 151.85 km/s and 150.27 km/s, respectively. In Figure 10 (c), we
 577 show the calculated diameters of the identified plasmoids by multiplying the Alfvén speed (b) with
 578 the peak-to-peak duration (Δt) for each event. The spacecraft travel distance (Δx) during the Δt
 579 time was also accounted for, although it is negligible compared to the plasmoid motion. Also
 580 shown in Figure 10 (c) is the ion-inertial length as a function of radial distance, calculated based
 581 on the same density profile. An ion mass of 16 amu was assumed for the calculations due to the
 582 dominance of heavy ions ($O^+/S^+/S^{++}$) in the Jovian magnetosphere. Figure 10 (c) illustrates that
 583 the diameters of all events with in-situ signatures shorter than 5 minutes are within an order of
 584 magnitude of the local ion inertial length, with some events having diameters even shorter than
 585 this length scale.

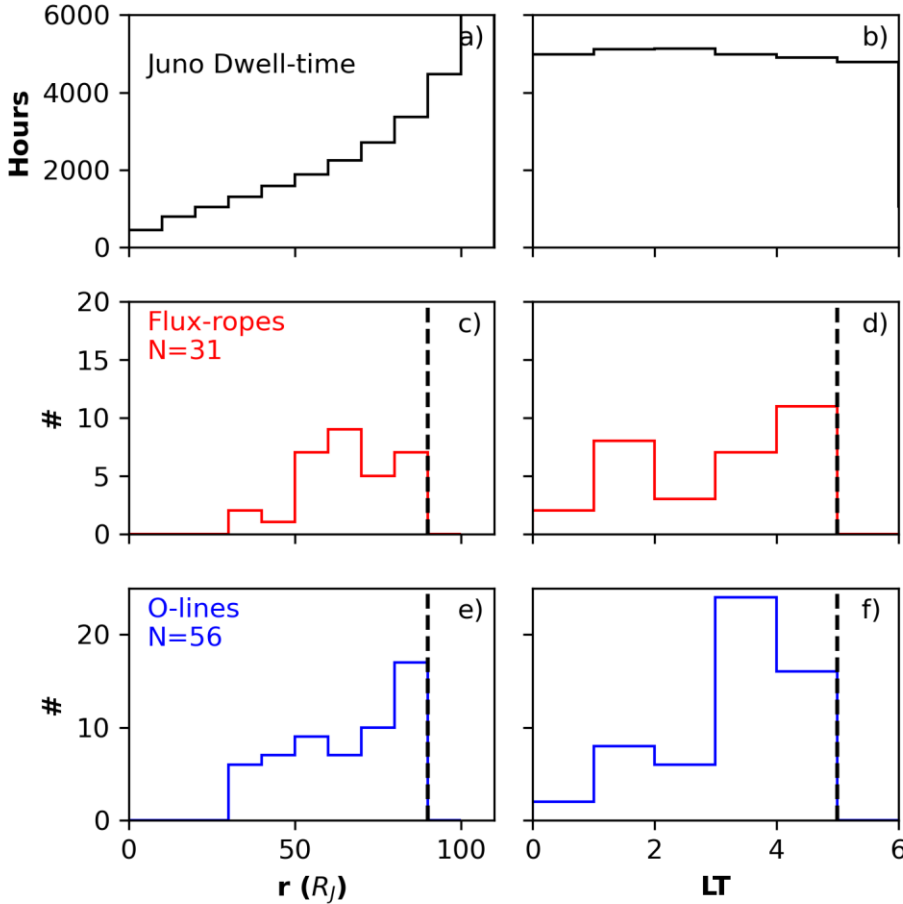
586 However, we note that defining the plasmoid duration between the two extrema in B_θ may
 587 lead to underestimation of the size of the plasmoid as the reversal alone does not account for the
 588 post-reversal post-plasmoid plasma sheet (PPPS) (Vogt et al., 2014; Cowley et al., 2015).

589 3.4. Relative occurrence of flux-ropes versus O-lines

590 For some plasmoids identified by the algorithm, we observed that an increase in the
 591 magnetic field strength near the center of the events i.e., near the reversal in B_θ , caused an
 592 increased in the component of the magnetic field in the direction of intermediate variance (B_M).
 593 However, these increases in B_M did not always correspond to an increase the overall magnetic field
 594 strength due to the near-zero values of the component of maximum variance (B_L) near the center
 595 of the event as it reversed sign during the plasmoid interval. Hence, in our work, we classified
 596 those events as flux-ropes in which the median of the intermediate-variance component (B_M) was
 597 larger than that measured at the beginning and end of the event interval. In other cases, where there
 598 was no localized increase in B_M , the reversal of the magnetic field usually resulted in a minimum
 599 field strength at the center of the event interval; such events were classified as magnetic O-lines.
 600 Out of 87 plasmoids events identified by the algorithm, 31 were classified as magnetic flux-ropes
 601 and 56 were classified as magnetic O-lines.

602 Figure 11 shows the distributions of flux-ropes and O-lines identified by the algorithm in
 603 radial distance and local time. Out of the 31 flux-ropes, 28 were found at radial distances beyond
 604 50 R_J . Similarly, out of 56 O-lines, 43 were observed beyond 50 R_J , which could be due to the
 605 longer time spent by Juno in distances beyond 50 R_J . The greatest number of O-lines were observed
 606 between 80 and 90 R_J (N=18), whereas flux-ropes were found likely to occur between 50 and 90

607 R_J. More flux-ropes and O-lines were observed near the dawn-side magnetotail (03-05 LT) than
 608 near midnight (00-02 LT). This could be due to Juno's orbit, as between 00 and 02 LT it only
 609 crossed the current sheet at radial distances inward of 50 R_J, which could be planetward of the
 610 reconnection X-line in these local times.



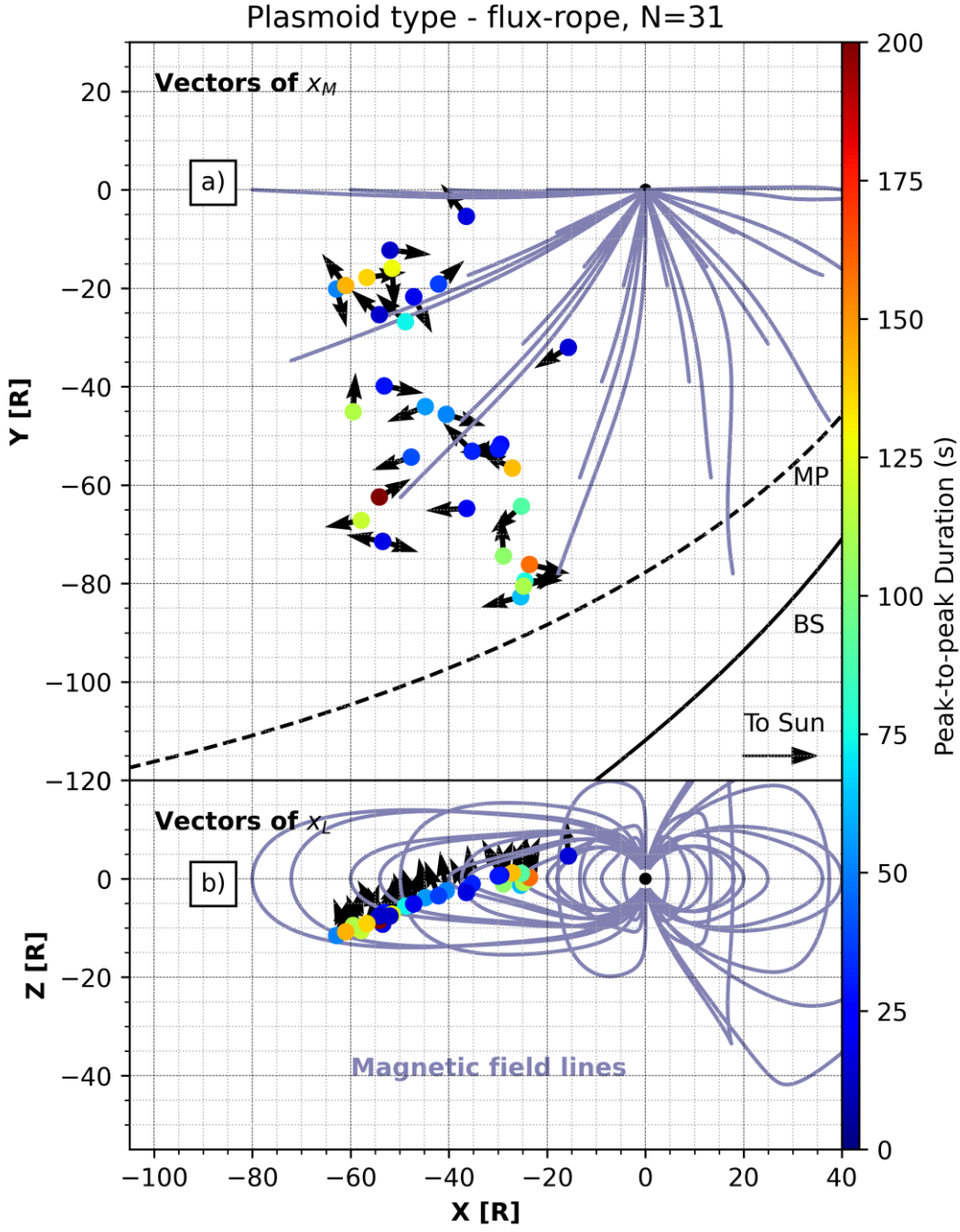
611

612 **Figure 11.** Histograms of the locations of the identified flux-rope and O-line events in radial
 613 distance and local time. Time spent by the Juno spacecraft in each bin is shown in panels a) and
 614 b). The dashed lines mark the limits of the detection algorithm.

615 The direction of the core field for a magnetic flux-rope is closely associated with the MVA
 616 eigenvector corresponding to the direction of intermediate variance (\vec{x}_M), which is illustrated in
 617 Figure 12 for all 31 flux-rope events. Also shown in Figure 12 are representative magnetic field
 618 lines from the Sarkango et al., (2019) MHD model which show the bend-back of the magnetic
 619 field lines due to the sub-corotation of the magnetospheric plasma. The flux-rope events were
 620 observed at nearly all local times sampled by Juno, with a wide range of core field orientations.
 621 Also shown in Figure 12 (b) are the eigenvectors corresponding to the direction of maximum
 622 variance (\vec{x}_L), which should be predominantly in the north-south direction as it was the basis on
 623 which these events were identified.

624 For an O-line, the direction of minimum variance of the field is used to infer the core-field
 625 direction as the intermediate variance is expected to be close to the radial direction. Figure 13
 626 shows the MVA eigenvectors corresponding to the direction of minimum variance (\vec{x}_N) (top) and

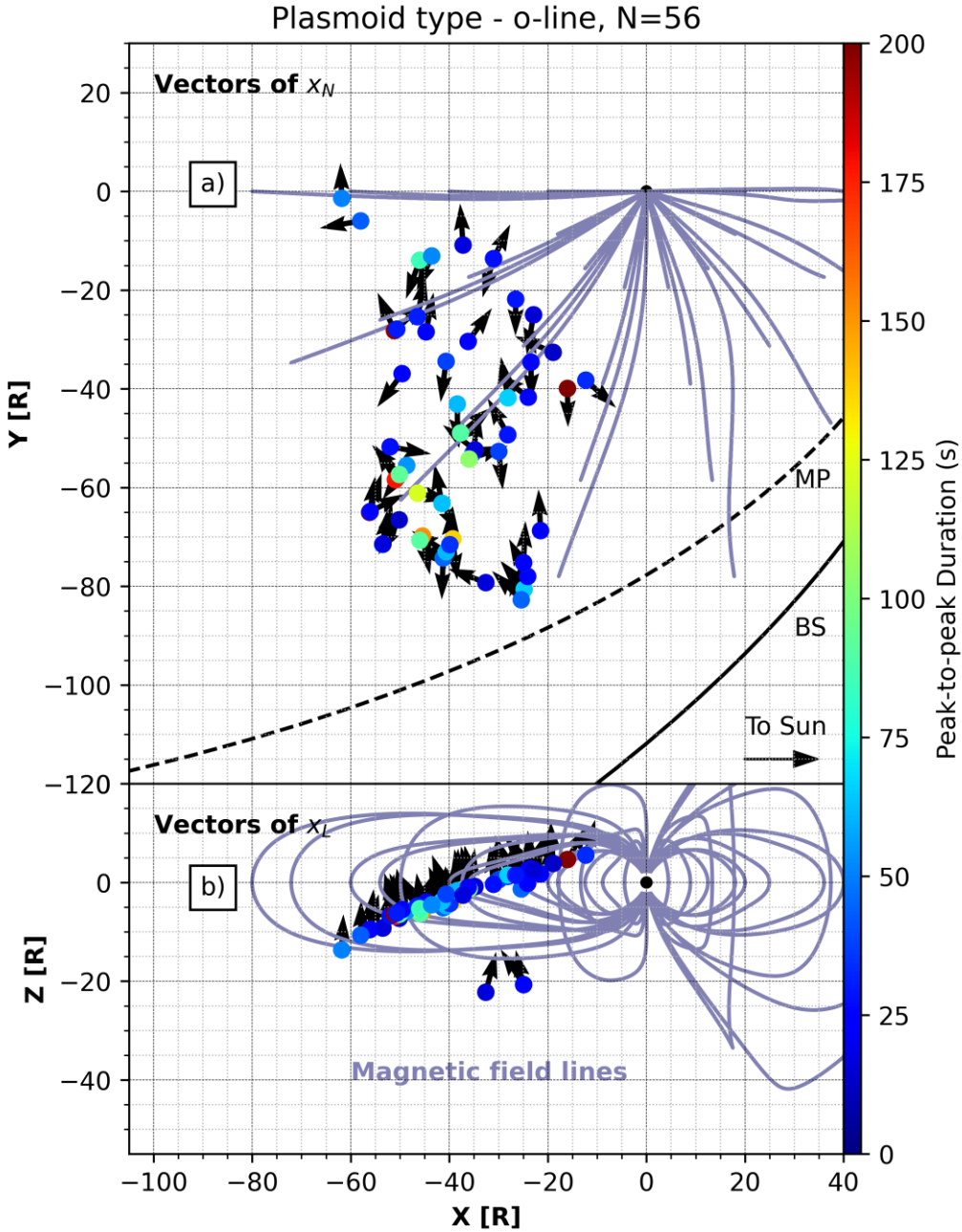
maximum variance (\vec{x}_L) for all 56 O-line events in a similar format as Figure 12. As for the flux-ropes, O-lines were observed at nearly all local times between 00 and 05 and had a wide range of core field orientations compared to the local bend-back direction. For both flux-ropes and O-lines, the direction of maximum variance was close to the Z direction in the JSS coordinate system.



631

632 **Figure 12.** Eigenvectors of the intermediate and maximum variance shown in the equatorial and
 633 meridional projections for the 31 flux-rope events identified by the algorithm. Each event is
 634 colored according to its peak-to-peak duration. Also shown in blue are magnetic field lines from
 635 an MHD model.

636

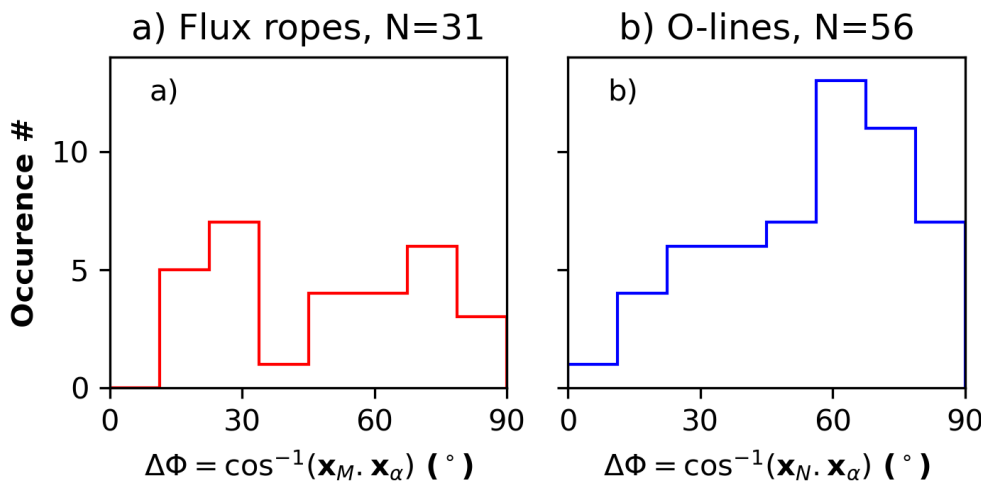


637

638 **Figure 13.** Eigenvectors of the minimum and maximum variance shown in the equatorial and
 639 meridional projections for the 56 O-line events identified by the algorithm. Each event is colored
 640 according to its peak-to-peak duration. Also shown in blue are magnetic field lines from an
 641 MHD model.

642 We compared the core-field directions of the flux-ropes and the O-lines with the local bend-
 643 back plane, which is presumably also the plane in which reconnection is occurring. The plane of
 644 the bend-back for each plasmoid events was determined by calculating the average of $\alpha = \tan^{-1}(B_\phi/B_r)$
 645 for a 10-minute period starting 20 minutes prior to the observed B_θ reversal, during
 646 which time the spacecraft was typically sampling the off-equatorial / mid-latitudes, as seen in the

647 anti-correlated azimuthal (B_ϕ) and radial (B_r) components of the magnetic field. In Figure 14, we
 648 show the angle between the core-field direction and the vector intersecting the local bend-back
 649 plane and the JSS equatorial plane (\vec{x}_α). The direction of intermediate variance was chosen as the
 650 core-field direction for the magnetic flux-rope events whereas the minimum variance direction
 651 was chosen for the O-lines. Near 90° values of $\Delta\phi$ imply that the axial direction of the plasmoid
 652 was perpendicular to the bend-back plane, which is predominantly the case for O-lines, which
 653 show preferences for larger acute angles. Such a result is very consistent with the configuration of
 654 O-lines formed in the midnight-to-dawn quadrant in the global simulation of Saturn's
 655 magnetosphere by Jia et al., (2012). Although more flux-ropes were seen with $\Delta\phi > 45^\circ$ (N=19)
 656 than vice-versa (N=13), the histograms show that angles between $20\text{--}30^\circ$ were as likely to occur
 657 as those between $70\text{--}80^\circ$.



658

659 **Figure 14.** Histograms showing the acute angle between the core-field direction and the local
 660 bend-back plane for a) flux-ropes and b) O-lines identified by the algorithm.

661 A constant- α force-free flux-rope model was fitted to each flux-rope event (N=31) based
 662 on the methodology described in Section 2.5. Out of the 31 which were originally classified as
 663 flux-ropes, 6 produced reduced-chi-squared errors less than 0.3 nT^2 for an average field strength
 664 between 2 and 6 nT, which suggests that they were close to being force-free.

665 4. Discussion

666 4.1. Ion-inertial scale plasmoids in the Jovian magnetotail

667 The magnetic flux rope event shown in Figure 3 lasted approximately 61 s between the two
 668 extrema in B_θ , which roughly corresponds to a plasmoid diameter of 17141 km, assuming it
 669 travelled at the Alfvén speed of ~ 281 km/s corresponding to that in the surrounding magnetotail
 670 lobes ($B=4$ nT, $n_{\text{lobe}}=0.006 \text{ cm}^{-3}$, based on Waves data). This diameter was roughly 2 times the
 671 local ion inertial length, which we calculated to be ~ 8178 km (assuming quasi-neutrality and ion
 672 mass of 16 amu). The second example, shown in Figure 5, had a ‘peak-to-peak’ duration of 63 s.
 673 The magnetic field strength in the surrounding lobes was approximately 5 nT, which corresponds
 674 to an Alfvén speed of ~ 498 km/s (for $n_{\text{lobe}}=0.003 \text{ cm}^{-3}$) and a plasmoid diameter of ~ 31374 km.

675 The ion inertial length during this interval was also \sim 11683 km, making the plasmoid
 676 approximately 2.68 times larger than this length scale.

677 Figure 9 and Figure 10 illustrate the scale of the plasmoids detected by the algorithm using
 678 similar calculations. A majority ($N=50$ out of 87) of plasmoids were seen to last less than 60 s,
 679 measured between the peaks in B_θ . In contrast, previous surveys (Figure 9 (b)) have discussed
 680 larger plasmoids with durations longer than 2 min. In Figure 10, we calculated the diameters of
 681 the plasmoids based on the ‘peak-to-peak’ duration and the Alfvén speed in the lobes and
 682 demonstrate that the diameters of all events were within one order of magnitude of the local oxygen
 683 ion-inertial length. Our survey demonstrates that reconnection occurs in the Jovian magnetotail at
 684 kinetic scales and produces ion-inertial scale plasmoids, like in other regions in the space
 685 environments such as the terrestrial magnetotail. Numerical simulations of ion-scale plasmoids
 686 have shown that they evolve by interacting with other plasmoids , i.e., via coalescence, which
 687 could ultimately produce the large plasmoids analyzed by previous surveys.

688 Our calculations of plasmoid diameters are subject to the assumption that the ‘peak-to-
 689 peak’ signature represents the entire plasmoid crossing. However, limiting the plasmoid duration
 690 between the two extrema in B_θ may underestimate the plasmoid size by a factor of 4 or more (Vogt
 691 et al., 2014). Note that we have used a mass of 16 amu or the mass of O^+ for the average mass of
 692 singly charged ions. Due to the abundance of singly charged sulfur ions, the ion inertial length in
 693 the Jovian magnetotail may be even larger than the numbers described above, which further
 694 supports our conclusions that our identified small-scale plasmoids have spatial sizes comparable
 695 to the local ion inertial length.

696 Our observations show that reconnection in Jupiter’s magnetotail may be proceeding via
 697 current-sheet instabilities, as found in other magnetospheres The tearing instability is most likely
 698 to occur in a thin current sheet. In the magnetotail, this depends on the ratio of the radial field in
 699 the lobes ($B_{r,lobe}$) and the meridional field at the equator ($B_{\theta,equator}$) (Kronberg et al., 2007),
 700 which changes over the course of the large-scale loading of the magnetosphere. Hence, on a global
 701 scale, there are no different onset conditions for the small-scale reconnection events. However, as
 702 smaller plasmoids with diameters roughly between \sim 10,000 to 50,000 km are easier to miss being
 703 detected by a single spacecraft in the magnetotail, the observations presented here raise new
 704 questions about the frequency at which reconnection occurs and whether it could also be occurring
 705 in other regions of the magnetosphere, such as the dusk side magnetotail.

706 **4.2. Abundance of O-lines versus flux-ropes**

707 On comparing the Waves electric field spectra for Example 1 (Figure 3 (e)), we observe
 708 that the cutoff for the continuum radiation briefly decreased from 1.1kHz to 0.9 kHz within the
 709 plasmoid event. This minor transient decrease was different from the larger increase in the cutoff
 710 frequency (from 500 Hz to 1 kHz) over the broader interval containing the plasmoid event, and
 711 the latter could a result of Juno entering the dense plasmasheet. The transient decrease in the cutoff
 712 frequency indicates a decrease in the plasma density within the plasmoid. The magnetic field
 713 strength increased within the event due to the core field, which led us to classify it as a magnetic
 714 flux-rope. Hence, the density decrease observed by Waves is consistent with the result that
 715 Example 1 was a flux-rope where the magnetic tension of the outer wraps is balanced by the larger
 716 magnetic pressure in the interior. However, this flux-rope was not entirely force-free, as discussed
 717 in Section 3.1.1.

718 The cutoff briefly increased to higher frequencies for Example 2 (Figure 5 (e)) from 500
 719 Hz to 700 Hz, indicating that the plasma frequency and electron density also increased.
 720 Simultaneously, the magnetic field strength decreased within the interval. This supports our
 721 interpretation that the second plasmoid (Figure 5 and Figure 6) was an O-line, and the magnetic
 722 pressure of the outer helical structure was balanced by the larger thermal pressure contained within
 723 the plasmoid core. The relatively high cutoff frequency of ~1 kHz and corresponding higher
 724 density were also seen after the reversal in the post-plasmoid plasma sheet.

725 Like the Vogt et al., (2014) survey for Jupiter and the Jackman et al., (2011) survey for
 726 Saturn, we find that a majority of B_θ reversals associated with a plasmoid event do not have strong
 727 core fields. Out of the total 87 plasmoid candidates only 31 can be classified as magnetic flux-
 728 ropes, and out of these only 6 were found to fit the force-free model well with χ^2_r less than 0.3 nT².
 729 This could be because the plasmoids are generated within a high β plasma, where plasma pressure
 730 gradients are very large. Dense plasma inside plasmoids could increase the thermal pressure which
 731 would oppose the magnetic tension of the outer helical wraps (Kivelson & Khurana, 1995). In
 732 contrast, the abundance of flux-ropes seen in the terrestrial-like magnetospheres could also be
 733 because of the stronger cross-magnetotail magnetic field introduced by the IMF (Slavin et al.,
 734 2003), which has a weaker, if not negligible, influence in the Jovian magnetosphere as the
 735 magnetopause reconnection is relatively weak. In the terrestrial case, the northern and southern
 736 magnetotail lobes are sheared due to the solar wind interaction (Cowley, 1981), which can
 737 contribute to a core-field for a plasmoid structure. (Here ‘sheared’ refers to the displacement of
 738 the two lobes with respect to each other, rather than to the anti-parallel magnetic field across the
 739 current sheet). Meanwhile, at Jupiter, the northern and southern lobes are not sheared, though the
 740 entire reconnection plane is likely skewed due to the bend-back effect (Russell et al., 1998). This
 741 could also result in more O-lines being generated than flux-ropes at Jupiter and Saturn.

742 Results of the minimum variance analysis on all flux-rope and O-line events showed that
 743 their core fields can be highly skewed in the XY plane (Figure 12 and Figure 13). In an ideal
 744 scenario, the core field of a newly produced plasmoid would be perpendicular to the plane of
 745 reconnection. In the Jovian magnetotail, this is determined by the ‘bend-back’ of the magnetic
 746 field lines due to sub-corotation of the plasma. So, it is interesting to compare the core field
 747 directions with the orientation of the local bend-back plane. In Figure 14 we showed the angle
 748 between these two vectors. The majority (~70%) of O-line events identified by our algorithm have
 749 core fields which are oriented larger than 45° from the bend-back plane. A similar but less
 750 prominent result is found for the flux-ropes, ~60% of which subtend angles larger than 45° with
 751 respect to the bend-back plane.

752 In Figure 11 we showed the occurrence of flux-ropes and O-lines detected by our algorithm
 753 at different radial distances and local times. Both flux-ropes and O-lines were seen more frequently
 754 at larger radial distances due to Juno’s orbital bias. However, very few flux-ropes were seen at
 755 distances inward of 50 R_J, while O-lines were equally likely to occur at all bins between 30 and
 756 70 R_J, though they are most likely between 70 and 90 R_J. Assuming that flux-ropes are plasmoids
 757 at a later stage during their evolution than O-lines, it is plausible that their signatures would be
 758 seen more frequently for regions in the deep magnetotail. Conversely, O-lines, which contain
 759 dense plasma and are possibly products of fresh reconnection, are more likely to occur closer to
 760 the planet.

761 4.3. Contribution of small-scale plasmoids to mass loss from the magnetosphere

762 We can produce cursory estimates of the mass carried by a small-scale plasmoid by
 763 assuming that it occupies a cylindrical volume with diameter equal to the average calculated in our
 764 survey, $\sim 10,000$ km and possesses a uniform density of 0.05 cm^{-3} . Consider three additional
 765 parameters: f , a factor to scale the plasmoid diameter to obtain the cross-tail dimension, \dot{M} , the
 766 net mass loss rate due to plasmoids, and δt , the time duration between two consecutive plasmoid
 767 events. With $f = 10$ (plasmoid cross tail length equal to 10 times its diameter), one plasmoid with
 768 cross-sectional diameter of 10000 km would need to be released every $\delta t = 0.1$ s to provide a
 769 total mass loss rate $\dot{M} = mnV/\delta t$ (where V is the plasmoid volume) equal to 100 kg/s. Note that
 770 the actual plasmoid-related mass loss deficit is > 500 kg/s, which is even larger. Plasmoids which
 771 were released at such high frequencies would have been detected more often by Juno, which spent
 772 more than 150 hours at distances less than 10,000 km to the current sheet.

773 In the above calculation, the assumed plasmoid diameter is $0.13 R_J$. In contrast, Cowley et
 774 al., (2015) assumed dimensions of $\sim 150 R_J$ in the tailward direction, $\sim 70 R_J$ in the cross-tail
 775 direction and $\sim 7 R_J$ for the direction normal to the current sheet plane. They argue that the large
 776 tailward dimensions of the plasmoid are due to the post-plasmoid plasma sheet, which is present
 777 in the reconnection exhaust.

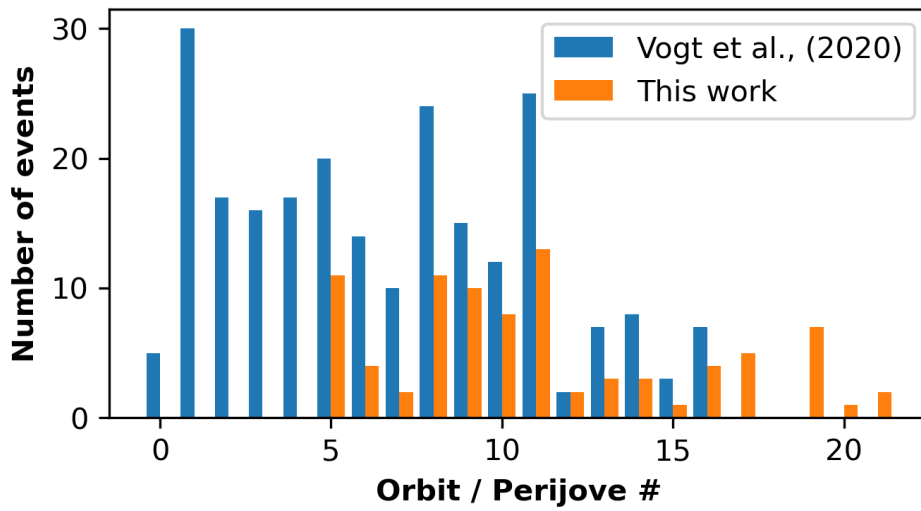
778 An alternative approach is to evaluate the effective outflow area needed to lose 1 ton/s of
 779 mass continuously, e.g., via steady reconnection instead of sporadic plasmoid release. If we
 780 assume the density at $\sim 80 R_J$ downstream is $\sim 0.01 \text{ cm}^{-3}$ and the outflow speed is $\sim 400 \text{ km/s}$, a
 781 total area of $\sim 1828 R_J^2$ would be needed to lose 1 ton of mass per second. This translates to a square
 782 region $\sim 42.7 R_J$ in length on each side. The area and square length reduce to $366 R_J^2$ and $19.1 R_J$ if
 783 the density is increased by a factor of 5. Since observations have shown that reconnection in the
 784 Jovian magnetotail does not appear to occur in a steady manner, and a period of several days passes
 785 between consecutive large-scale ‘unloading’ events, the combined dimensions (in at least two
 786 directions) of all plasmoids in an ‘unloading’ interval must be larger than the length scales needed
 787 for continuous outflow of plasma, if they must account for all 1 ton/s of production.

788 Hence, the conclusion from this discussion is that small-scale magnetic reconnection does
 789 not contribute in a substantial manner to mass loss from the Jovian magnetosphere, and only large
 790 plasmoids with a prolonged PPPS may potentially account for the loss of 1 ton/s of mass from the
 791 magnetosphere. Other loss mechanisms apart from magnetic reconnection are out of scope of the
 792 present work and are not discussed here.

793 4.4. Orbit-by-orbit variability and comparison with other studies

794 The number of plasmoid events identified by our algorithm varied between perijove passes
 795 or Juno orbits. It has been shown by Vogt et al., (2020) and Yao et al., (2019) that some orbits
 796 were more “active” than others, in the form of frequent in situ sightings of magnetic reconnection
 797 or of more dynamic aurora. We found a similar result, and in Figure 15 we compare the occurrence
 798 of the plasmoids presented in this survey with the reconnection events identified by Vogt et al.,
 799 (2020) for different Juno perijoves. Both surveys show excellent agreement with each other. Orbit
 800 5, 8, 9, 10, and 11 were especially active. On the other hand, fewer events were seen for orbit 7,
 801 and for orbit numbers beyond 12. The latter could perhaps be explained by Juno’s increasing
 802 inclination and lack of sampling of larger radial distances (Section 2.1). The orbital bias is less

803 prominent for adjacent perijoves like 6 and 7 which nevertheless show different levels of activity.
 804 This variation on time scales longer than fluctuations in the upstream solar wind conditions could
 805 be explained by a different internal magnetospheric state, e.g., due to changes in Io's volcanic
 806 activity. The two example plasmoid events discussed in Section 3.1 were observed by Juno on
 807 DOY 75 and 76, 2017 during orbit 5 within a longer period of unloading of the magnetosphere,
 808 which was discussed by Yao et al., (2019). They also noted that the UV aurora was dimmer during
 809 orbit 7 than orbit 5. The long-term variability of the Jovian magnetosphere may be linked to other
 810 visible changes such as in the strength of the magnetodisc current sheet and location of the Jovian
 811 aurora, which could occur due to changes in mass loading from Io rather than external solar wind
 812 conditions (Vogt et al., 2017).



813

814 **Figure 15.** Histograms showing the occurrence of reconnection events in the Vogt et al., (2020)
 815 survey and of plasmoid events in our present work for different Juno orbits or perijoves. Orbits 4
 816 and below were excluded from the present work.

817 5. Conclusions

818 In this work, we used data from the Juno spacecraft to identify plasmoids in the Jovian
 819 magnetotail with in situ durations on the order of 5 minutes or less. These small-scale events have
 820 diameters comparable to the ion inertial length, which is an important length scale as it is related
 821 to the size of the ion diffusion region in magnetic reconnection. We used data from the Juno
 822 magnetometer to identify reversals in the north-south component of the magnetic field, which is
 823 expected to occur in a reconfiguration of the magnetotail during magnetic reconnection. An
 824 automated algorithm is applied to detect B_θ reversals and identify corresponding extrema which
 825 determine the start and end of the event. Various filters are applied during the detection procedure
 826 based on the minimum variance analysis and other magnetic properties such as the proximity to
 827 the current sheet and the magnitude of the perturbation associated with the event. Based on our
 828 algorithm, we detected 87 plasmoids with 'peak-to-peak' durations between 10 s and 5 min, out
 829 of which 31 were seen to have an increase in the field component normal to the reconnection plane
 830 and were classified as magnetic flux-ropes, while the 56 events with minimum field strengths at
 831 their centers were classified as magnetic O-lines.

We examined two such plasmoid events in more detail due to the availability of simultaneous, higher cadence energetic particle intensities measured by the JEDI instruments. The results of the minimum variance analysis show that the first event can be classified as a magnetic flux-rope whereas the second had minimum field strength at its center and was an O-line. Energetic particle fluxes were seen to maximize for the second plasmoid event for the electrons, protons, oxygen and sulfur ions. Moreover, the electron pitch angle spectra indicate isotropic distributions within the magnetic loop structure, which could be due to betatron acceleration either at the front of, or within the plasmoid. For the second event, the isotropic pitch-angle distribution gradually tends to become field-aligned in the proximity of the plasmoids.

We used the ‘peak-to-peak’ duration between the two extrema in B_θ to calculate the duration for each plasmoid event identified by the algorithm. Within the interval of 10 s and 5 min chosen for the algorithm, a majority of plasmoids ($N=50$ out of 87) were seen with durations lasting less than 60 s. It is interesting to compare the distribution of plasmoid durations with previous surveys (Kronberg, Woch, Krupp, & Lagg, 2008; Vogt et al., 2014). Although the two previous studies used different definitions to define a plasmoid and looked for signatures on different timescales, their histograms also showed a similar behavior. In both studies, the histograms were skewed toward smaller values, indicating that smaller plasmoids were more likely to be observed, depending on the length scales under consideration. Similar results have also been reported for flux-ropes observed in the solar wind (Hu et al., 2018), and for plasmoids seen in Saturn’s magnetosphere (Garton et al., 2021), which have shown that plasmoid diameters exhibit a power-law-like scaling. The duration of the 87 plasmoids observed in our survey is also used to estimate the plasmoids’ diameters using the lobe Alfvén speed. We demonstrate that all events with durations less than 5 minutes can have diameters within an order of magnitude larger or smaller than the local ion-inertial length. These results demonstrate that magnetic reconnection occurs in the Jovian magnetotail at ion kinetic scales, like in other regions in the space environments. This is important as multiple ion-inertial scale plasmoids can coalesce to form larger plasmoids, such as those analyzed by previous studies, and can also trap and accelerate ions and electrons.

The abundance of O-lines ($N=56$) versus flux-ropes ($N=31$) identified by the algorithm is consistent with previous surveys of plasmoids in Jupiter’s (Vogt et al., 2014) and Saturn’s (Jackman et al., 2011) magnetotail. Using the minimum variance analysis, we show that O-lines detected by our algorithm were more likely to have an axial direction perpendicular to the reconnection plane, which in the case of the Jovian magnetotail is assumed to be the local plane of bent-back magnetic field. The core-fields for the flux-ropes do not show a clear relationship with the bend-back plane, which could be because flux-ropes structures are at a later stage of plasmoid evolution and are ‘de-coupled’ from the corotation dynamics that cause the bend-back. Alternatively, the small number of flux ropes formed at Jupiter may simply be due to the weakness of the IMF at 5.2 AU combined with vast dimensions of this huge magnetosphere. As a result, reconnection deep in Jupiter’s magnetosphere may not be aware of the direction of the IMF and any shearing of the two tail lobes due to IMF stress may be extremely weak. Such a situation may well favor the development of O-lines as opposed to flux-ropes. In contrast, in terrestrial-like magnetospheres like those of Earth and Mercury, the IMF B_Y component is an important factor to produce the core field of the plasmoid.

Despite being smaller, 87 ion-inertial scale plasmoids were detected by Juno and captured by our algorithm. We demonstrate that a plasmoid with a cross-sectional diameter of 10,000 km ($= 0.13 R_J$) and density of 0.5 cm^{-3} would need to be released at least once every 0.1 s to result in

877 a 100 kg/s loss rate. We argue that this release frequency is unlikely since Juno would have
 878 detected more such events had it been the case. Based on cursory calculations, we argue also that
 879 the total dimensions of plasmoids in at least two dimensions must be larger than several tens of R_J
 880 to match the dimensions of an effective outflow area needed to lose 1 ton/s of mass. This may
 881 become possible if the post-plasmoid plasma sheet is included in the calculations, as argued by
 882 Cowley et al., (2015). Hence, we suggest that ion-inertial scale plasmoid release, by itself, is an
 883 insignificant loss mechanism, unless several hundred such events are produced simultaneously
 884 every 1 s or less, which is unlikely according to the current observations.

885 Lastly, we compare the events detected by our algorithm with the survey of reconnection
 886 signatures observed by Vogt et al., (2020). The relative occurrence of plasmoid and reconnection
 887 events show a very good agreement and both studies find different magnetospheric behavior for
 888 different yet consecutive Juno orbits. For example, in both studies, the number of reconnection
 889 signatures seen during Juno orbit #8 were less than half of the total number seen during orbit #9.
 890 The mechanisms which can lead to such variability over the long timescale associated with each
 891 orbit (~53 days), need to be examined further.

892 Acknowledgments, Samples, and Data

893 This work was supported by NASA through the NASA Earth and Space Science Fellowship
 894 Grant 80NSSC17K0604 and Early Career Fellow Startup Grant 80NSSC20K1286. The research
 895 at the University of Iowa is supported by NASA through contract 699041X with the Southwest
 896 Research Institute. The Juno magnetometer (MAG), Waves and JEDI data used in this study is
 897 publicly available from the Planetary Plasma Interactions node of the Planetary Data System at
 898 <https://pds-ppi.igpp.ucla.edu/>.

899 References

- 900 Artemyev, A. V., Kasahara, S., Ukhorskiy, A. Y., & Fujimoto, M. (2013). Acceleration of ions
 901 in the Jupiter magnetotail: Particle resonant interaction with dipolarization fronts. *Planetary*
 902 and *Space Science*, 82–83, 134–148. <https://doi.org/10.1016/j.pss.2013.04.013>
- 903 Artemyev, A. V., Clark, G., Mauk, B., Vogt, M. F., & Zhang, X. J. (2020). Juno Observations of
 904 Heavy Ion Energization During Transient Dipolarizations in Jupiter Magnetotail. *Journal of*
 905 *Geophysical Research: Space Physics*, 125(5), 1–14. <https://doi.org/10.1029/2020JA027933>
- 906 Bagenal, F. (2007). The magnetosphere of Jupiter: Coupling the equator to the poles. *Journal of*
 907 *Atmospheric and Solar-Terrestrial Physics*, 69(3), 387–402.
 908 <https://doi.org/10.1016/j.jastp.2006.08.012>
- 909 Bagenal, F., & Delamere, P. A. (2011). Flow of mass and energy in the magnetospheres of
 910 Jupiter and Saturn. *Journal of Geophysical Research: Space Physics*, 116(5).
 911 <https://doi.org/10.1029/2010JA016294>
- 912 Barnhart, B. L., Kurth, W. S., Groene, J. B., Faden, J. B., Santolik, O., & Gurnett, D. A. (2009).
 913 Electron densities in Jupiter's outer magnetosphere determined from Voyager 1 and 2
 914 plasma wave spectra. *Journal of Geophysical Research: Space Physics*, 114(5), 5218.
 915 <https://doi.org/10.1029/2009JA014069>
- 916 Connerney, J. E. P., Benn, M., Bjarno, J. B., Denver, T., Espley, J., Jorgensen, J. L., et al. (2017).
 917 The Juno Magnetic Field Investigation. *Space Science Reviews*.

- 918 <https://doi.org/10.1007/s11214-017-0334-z>
- 919 Cowley, S. W. H. (1981). Magnetospheric asymmetries associated with the y-component of the
920 IMF. *Planetary and Space Science*, 29(1), 79–96. [https://doi.org/10.1016/0032-0633\(81\)90141-0](https://doi.org/10.1016/0032-0633(81)90141-0)
- 922 Cowley, S. W. H., Nichols, J. D., & Jackman, C. M. (2015). Down-tail mass loss by plasmoids in
923 Jupiter's and Saturn's magnetospheres. *Journal of Geophysical Research A: Space Physics*,
924 120(8), 6347–6356. <https://doi.org/10.1002/2015JA021500>
- 925 Delamere, P. A., & Bagenal, F. (2013). Magnetotail structure of the giant magnetospheres:
926 Implications of the viscous interaction with the solar wind. *Journal of Geophysical
927 Research: Space Physics*, 118(11), 7045–7053. <https://doi.org/10.1002/2013JA019179>
- 928 Drake, J. F., Swisdak, M., Che, H., & Shay, M. A. (2006). Electron acceleration from contracting
929 magnetic islands during reconnection. *Nature*, 443(7111), 553–556.
930 <https://doi.org/10.1038/nature05116>
- 931 Garton, T. M., Jackman, C. M., & Smith, A. W. (2021). Kronian Magnetospheric Reconnection
932 Statistics Across Cassini's Lifetime. *Journal of Geophysical Research: Space Physics*,
933 126(8), e2021JA029361. <https://doi.org/10.1029/2021JA029361>
- 934 Ge, Y. S., Jian, L. K., & Russell, C. T. (2007). Growth phase of Jovian substorms. *Geophysical
935 Research Letters*, 34(23), 1–6. <https://doi.org/10.1029/2007GL031987>
- 936 Ge, Y. S., Russell, C. T., & Khurana, K. K. (2010). Reconnection sites in Jupiter's magnetotail
937 and relation to Jovian auroras. *Planetary and Space Science*, 58(11), 1455–1469.
938 <https://doi.org/10.1016/j.pss.2010.06.013>
- 939 Grigorenko, E. E., Malykhin, A. Y., Kronberg, E. A., Malova, K. V., & Daly, P. W. (2015).
940 Acceleration of ions to suprathermal energies by turbulence in the plasmoid-like magnetic
941 structures. *Journal of Geophysical Research A: Space Physics*, 120(8), 6541–6558.
942 <https://doi.org/10.1002/2015JA021314>
- 943 Gurnett, D. A., Scarf, F. L., Kurth, W. S., Shaw, R. R., & Poynter, R. L. (1981). Determination
944 of Jupiter's electron density profile from plasma wave observations. *Journal of Geophysical
945 Research: Space Physics*, 86(A10), 8199–8212. <https://doi.org/10.1029/JA086IA10P08199>
- 946 Hu, Q., Zheng, J., Chen, Y., le Roux, J., & Zhao, L. (2018). Automated Detection of Small-scale
947 Magnetic Flux Ropes in the Solar Wind: First Results from the Wind Spacecraft
948 Measurements . *The Astrophysical Journal Supplement Series*, 239(1), 12.
949 <https://doi.org/10.3847/1538-4365/aae57d>
- 950 Jackman, C. M., Slavin, J. A., & Cowley, S. W. H. (2011). Cassini observations of plasmoid
951 structure and dynamics: Implications for the role of magnetic reconnection in
952 magnetospheric circulation at Saturn. *Journal of Geophysical Research: Space Physics*.
953 <https://doi.org/10.1029/2011JA016682>
- 954 Jia, X., Hansen, K. C., Gombosi, T. I., Kivelson, M. G., Tóth, G., Dezeeuw, D. L., & Ridley, A.
955 J. (2012). Magnetospheric configuration and dynamics of Saturn's magnetosphere: A global
956 MHD simulation. *Journal of Geophysical Research: Space Physics*, 117(5).
957 <https://doi.org/10.1029/2012JA017575>
- 958 Joy, S. P., Kivelson, M. G., Walker, R. J., Khurana, K. K., Russell, C. T., & Ogino, T. (2002).

- 959 Probabilistic models of the Jovian magnetopause and bow shock locations. *Journal of*
 960 *Geophysical Research: Space Physics*, 107(A10). <https://doi.org/10.1029/2001JA009146>
- 961 Kasahara, S., Kronberg, E. A., Kimura, T., Tao, C., Badman, S. V., Masters, A., et al. (2013).
 962 Asymmetric distribution of reconnection jet fronts in the Jovian nightside magnetosphere.
 963 *Journal of Geophysical Research: Space Physics*, 118(1), 375–384.
 964 <https://doi.org/10.1029/2012JA018130>
- 965 Khurana, K. K., Kivelson, M. G., Vasylunas, V. M., Krupp, N., Woch, J., Lagg, A., et al.
 966 (2004). The Configuration of Jupiter's Magnetosphere (Chapter 24). *Jupiter: The Planet,*
 967 *Satellites and Magnetosphere*.
- 968 Kivelson, M. G., & Khurana, K. K. (1995). Models of flux ropes embedded in a harris neutral
 969 sheet: Force-free solutions in low and high beta plasmas. *Journal of Geophysical Research*,
 970 100(A12), 23637. <https://doi.org/10.1029/95ja01548>
- 971 Kivelson, M. G., & Southwood, D. J. (2005). Dynamical consequences of two modes of
 972 centrifugal instability in Jupiter's outer magnetosphere. *Journal of Geophysical Research:*
 973 *Space Physics*, 110(A12). <https://doi.org/10.1029/2005JA011176>
- 974 Krimigis, S. M., Carbary, J. F., Keath, E. P., Bostrom, C. O., Axford, W. I., Gloeckler, G., et al.
 975 (1981). Characteristics of hot plasma in the Jovian magnetosphere: Results from the
 976 Voyager spacecraft. *Journal of Geophysical Research: Space Physics*, 86(A10), 8227–
 977 8257. <https://doi.org/10.1029/JA086IA10P08227>
- 978 Kronberg, E. A., Woch, J., Krupp, N., Lagg, A., Khurana, K. K., & Glassmeier, K. H. (2005).
 979 Mass release at Jupiter: Substorm-like processes in the Jovian magnetotail. *Journal of*
 980 *Geophysical Research: Space Physics*, 110(A3), 1–10.
 981 <https://doi.org/10.1029/2004JA010777>
- 982 Kronberg, E. A., Glassmeier, K. H., Woch, J., Krupp, N., Lagg, A., & Dougherty, M. K. (2007).
 983 A possible intrinsic mechanism for the quasi-periodic dynamics of the Jovian
 984 magnetosphere. *Journal of Geophysical Research: Space Physics*, 112(5).
 985 <https://doi.org/10.1029/2006JA011994>
- 986 Kronberg, E. A., Woch, J., Krupp, N., Lagg, A., Daly, P. W., & Korth, A. (2008). Comparison of
 987 periodic substorms at Jupiter and Earth. *Journal of Geophysical Research: Space Physics*,
 988 113(4), 1–11. <https://doi.org/10.1029/2007JA012880>
- 989 Kronberg, E. A., Woch, J., Krupp, N., & Lagg, A. (2008). Mass release process in the Jovian
 990 magnetosphere: Statistics on particle burst parameters. *Journal of Geophysical Research:*
 991 *Space Physics*, 113(10). <https://doi.org/10.1029/2008JA013332>
- 992 Kronberg, E. A., Grigorenko, E. E., Malykhin, A., Kozak, L., Petrenko, B., Vogt, M. F., et al.
 993 (2019). Acceleration of Ions in Jovian Plasmoids: Does Turbulence Play a Role? *Journal of*
 994 *Geophysical Research: Space Physics*, 124(7), 5056–5069.
 995 <https://doi.org/10.1029/2019JA026553>
- 996 Krupp, N., Woch, J., Lagg, A., Wilken, B., Livi, S., & Williams, D. J. (1998). Energetic particle
 997 bursts in the predawn Jovian magnetotail. *Geophysical Research Letters*, 25(8), 1249–1252.
 998 <https://doi.org/10.1029/98GL00863>
- 999 Krupp, N., Vasylunas, V. M., Woch, J., Lagg, A., Khurana, K. K., Kivelson, M. G., et al.

- 1000 (2004). Dynamics of the Jovian Magnetosphere. In *Jupiter. The planet, satellites and*
1001 *magnetosphere*.

1002 Kurth, W. S., Hospodarsky, G. B., Kirchner, D. L., Mokrzycki, B. T., Averkamp, T. F., Robison,
1003 W. T., et al. (2017). The Juno Waves Investigation. *Space Science Reviews*.
1004 <https://doi.org/10.1007/s11214-017-0396-y>

1005 Lepping, R. P., Jones, J. A., & Burlaga, L. F. (1990). Magnetic field structure of interplanetary
1006 magnetic clouds at 1 AU. *Journal of Geophysical Research*, 95(A8), 11957.
1007 <https://doi.org/10.1029/ja095ia08p11957>

1008 Masters, A. (2017). Model-Based Assessments of Magnetic Reconnection and Kelvin-Helmholtz
1009 Instability at Jupiter's Magnetopause. *Journal of Geophysical Research: Space Physics*,
1010 122(11), 11,154-11,174. <https://doi.org/10.1002/2017JA024736>

1011 Mauk, B. H., Haggerty, D. K., Jaskulek, S. E., Schlemm, C. E., Brown, L. E., Cooper, S. A., et
1012 al. (2013). The Jupiter Energetic Particle Detector Instrument (JEDI) Investigation for the
1013 Juno Mission. *Space Science Reviews* 2013 213:1, 213(1), 289–346.
1014 <https://doi.org/10.1007/S11214-013-0025-3>

1015 Moldwin, M. B., & Hughes, W. J. (1992). On the formation and evolution of plasmoids: A
1016 survey of ISEE 3 geotail data. *Journal of Geophysical Research: Space Physics*, 97(A12),
1017 19259–19282. <https://doi.org/10.1029/92JA01598>

1018 Nishida, A. (1983). Reconnection in the Jovian magnetosphere. *Geophysical Research Letters*,
1019 10(6), 451–454. <https://doi.org/10.1029/GL010i006p00451>

1020 Priest, E. R. (2011). The equilibrium of magnetic flux ropes (tutorial lecture). *Physics of*
1021 *Magnetic Flux Ropes (Eds C.T. Russell, E.R. Priest and L.C. Lee)*, 1–22.
1022 <https://doi.org/10.1029/gm058p0001>

1023 Rosa Oliveira, R. A., da Silva Oliveira, M. W., Ojeda-González, A., & De La Luz, V. (2020).
1024 New Metric for Minimum Variance Analysis Validation in the Study of Interplanetary
1025 Magnetic Clouds. *Solar Physics*, 295(3), 45. <https://doi.org/10.1007/s11207-020-01610-6>

1026 Russell, C. T., Khurana, K. K., Huddleston, D. E., & Kivelson, M. G. (1998). Localized
1027 reconnection in the near jovian magnetotail. *Science*, 280(5366), 1061–1064.
1028 <https://doi.org/10.1126/science.280.5366.1061>

1029 Sarkango, Y., Jia, X., & Toth, G. (2019). Global MHD simulations of the Response of Jupiter's
1030 Magnetosphere and Ionosphere to Changes in the Solar Wind and IMF. *Journal of*
1031 *Geophysical Research: Space Physics*, 124(7), 5317–5341.
1032 <https://doi.org/10.1029/2019JA026787>

1033 Sarkango, Y., Slavin, J. A., Jia, X., DiBraccio, G. A., Gershman, D. J., Connerney, J. E. P., et al.
1034 (2021). Juno Observations of Ion-Inertial Scale Flux Ropes in the Jovian Magnetotail.
1035 *Geophysical Research Letters*, 48(2). <https://doi.org/10.1029/2020GL089721>

1036 Slavin, J. A., Baker, D. N., Craven, J. D., Elphic, R. C., Fairfield, D. H., Frank, L. A., et al.
1037 (1989). CDAW 8 observations of plasmoid signatures in the geomagnetic tail: An
1038 assessment. *Journal of Geophysical Research*, 94(A11), 15153.
1039 <https://doi.org/10.1029/ja094ia11p15153>

1040 Slavin, J. A., Lepping, R. P., Gjerloev, J., Fairfield, D. H., Hesse, M., Owen, C. J., et al. (2003).

- 1041 Geotail observations of magnetic flux ropes in the plasma sheet. *Journal of Geophysical*
 1042 *Research: Space Physics*, 108(A1). <https://doi.org/10.1029/2002JA009557>
- 1043 Smith, A. W., Slavin, J. A., Jackman, C. M., Fear, R. C., Poh, G. K., DiBraccio, G. A., et al.
 1044 (2017). Automated force-free flux rope identification. *Journal of Geophysical Research: Space Physics*, 122(1), 780–791. <https://doi.org/10.1002/2016JA022994>
- 1045 Smith, A. W., Slavin, J. A., Jackman, C. M., Poh, G. K., & Fear, R. C. (2017). Flux ropes in the
 1046 Hermean magnetotail: Distribution, properties, and formation. *Journal of Geophysical Research: Space Physics*, 122(8), 8136–8153. <https://doi.org/10.1002/2017JA024295>
- 1047 Sonnerup, B. U. Ö., & Cahill, L. J. (1967). Magnetopause structure and attitude from Explorer
 1048 12 observations. *Journal of Geophysical Research*, 72(1), 171.
 1049 <https://doi.org/10.1029/jz072i001p00171>
- 1050 Taylor, J. B. (1974). Relaxation of toroidal plasma and generation of reverse magnetic fields.
 1051 *Physical Review Letters*, 33(19), 1139–1141. <https://doi.org/10.1103/PhysRevLett.33.1139>
- 1052 Vaivads, A., Khotyaintsev, Y. V., Retinò, A., Fu, H. S., Kronberg, E. A., & Daly, P. W. (2021).
 1053 Cluster Observations of Energetic Electron Acceleration Within Earthward Reconnection
 1054 Jet and Associated Magnetic Flux Rope. *Journal of Geophysical Research: Space Physics*,
 1055 126(8), 1–13. <https://doi.org/10.1029/2021ja029545>
- 1056 Vasyliunas, V. M. (1983). Plasma distribution and flow. In *Physics of the Jovian Magnetosphere*
 1057 (pp. 395–453). <https://doi.org/10.1017/cbo9780511564574.013>
- 1058 Vogt, M. F., Kivelson, M. G., Khurana, K. K., Joy, S. P., & Walker, R. J. (2010). Reconnection
 1059 and flows in the Jovian magnetotail as inferred from magnetometer observations. *Journal of Geophysical Research: Space Physics*, 115(6). <https://doi.org/10.1029/2009JA015098>
- 1060 Vogt, M. F., Jackman, C. M., Slavin, J. A., Bunce, E. J., Cowley, S. W. H., Kivelson, M. G., &
 1061 Khurana, K. K. (2014). Structure and statistical properties of plasmoids in Jupiter’s
 1062 magnetotail. *Journal of Geophysical Research A: Space Physics*, 119(2), 821–843.
 1063 <https://doi.org/10.1002/2013JA019393>
- 1064 Vogt, M. F., Bunce, E. J., Nichols, J. D., Clarke, J. T., & Kurth, W. S. (2017). Long-Term
 1065 Variability of Jupiter’s Magnetodisk and Implications for the Aurora. *Journal of Geophysical Research: Space Physics*, 122(12), 12,090–12,110.
 1066 <https://doi.org/10.1002/2017JA024066>
- 1067 Vogt, M. F., Connerney, J. E. P., DiBraccio, G. A., Wilson, R. J., Thomsen, M. F., Ebert, R. W.,
 1068 et al. (2020). Magnetotail Reconnection at Jupiter: A Survey of Juno Magnetic Field
 1069 Observations. *Journal of Geophysical Research: Space Physics*, 125(3).
 1070 <https://doi.org/10.1029/2019JA027486>
- 1071 Woch, J., Krupp, N., Lagg, A., Wilken, B., Livi, S., & Williams, D. J. (1998). Quasi-periodic
 1072 modulations of the Jovian magnetotail. *Geophysical Research Letters*, 25(8), 1253–1256.
 1073 <https://doi.org/10.1029/98GL00861>
- 1074 Woch, J., Krupp, N., Khurana, K. K., Kivelson, M. G., Roux, A., Perraut, S., et al. (1999).
 1075 Plasma sheet dynamics in the Jovian magnetotail: Signatures for substorm-like processes ?
 1076 *Geophysical Research Letters*, 26(14), 2137–2140. <https://doi.org/10.1029/1999GL900493>
- 1077 Woch, J., Krupp, N., & Lagg, A. (2002). Particle bursts in the Jovian magnetosphere: Evidence

- 1082 for a near-Jupiter neutral line. *Geophysical Research Letters*, 29(7), 42-1-42-4.
1083 <https://doi.org/10.1029/2001GL014080>
- 1084 Yao, Z. H., Grodent, D., Kurth, W. S., Clark, G., Mauk, B. H., Kimura, T., et al. (2019). On the
1085 Relation Between Jovian Aurorae and the Loading/Unloading of the Magnetic Flux:
1086 Simultaneous Measurements From Juno, Hubble Space Telescope, and Hisaki. *Geophysical
1087 Research Letters*, 46(21), 11632–11641. <https://doi.org/10.1029/2019GL084201>
- 1088 Yao, Z. H., Bonfond, B., Clark, G., Grodent, D., Dunn, W. R., Vogt, M. F., et al. (2020).
1089 Reconnection- and Dipolarization-Driven Auroral Dawn Storms and Injections. *Journal of
1090 Geophysical Research: Space Physics*, 125(8). <https://doi.org/10.1029/2019JA027663>
- 1091 Zhong, Z. H., Zhou, M., Tang, R. X., Deng, X. H., Turner, D. L., Cohen, I. J., et al. (2020).
1092 Direct Evidence for Electron Acceleration Within Ion-Scale Flux Rope. *Geophysical
1093 Research Letters*, 47(1), e2019GL085141. <https://doi.org/10.1029/2019GL085141>
- 1094